

Temperature limits for preservation of primary calcite clumped isotope paleotemperatures

Gregory A. Henkes^{a,*}, Benjamin H. Passey^a, Ethan L. Grossman^b,
Brock J. Shenton^b, Alberto Pérez-Huerta^c, Thomas E. Yancey^b

^a Department of Earth & Planetary Sciences, Johns Hopkins University, 3400 N. Charles St., 301 Olin Hall, Baltimore, MD 21218, United States

^b Department of Geology & Geophysics, Texas A&M University, MS 3115, College Station, TX 77843, United States

^c Department of Geological Sciences, The University of Alabama, Box 870338, Tuscaloosa, AL 35487, United States

Received 20 December 2013; accepted in revised form 23 April 2014; available online 14 May 2014

Abstract

Solid-state reordering of C–O bonds in the calcite lattice can alter the clumped isotope composition of paleotemperature archives such as fossil brachiopod shells without inducing significant changes in shell microstructure and trace element concentrations, metrics commonly used to gauge preservation quality. To correctly interpret the paleoenvironmental significance of clumped isotope-derived paleotemperatures, it is necessary to understand the temperature–time domain in which solid-state C–O bond reordering is important. We address this question using a combination of laboratory and natural geological experiments on Paleozoic brachiopod shells. The laboratory experiments involve heating fossil brachiopod calcite at different temperatures and times to directly observe rates of ^{13}C – ^{18}O bond reordering. The resulting Arrhenius parameters are indistinguishable from values previously determined for an optical calcite with similar trace element compositions. We develop an alternative kinetic model for reordering that accounts for non-first-order reaction progress observed during the initial several hundred minutes of laboratory heating experiments, and show that the simplified first-order approximation model (Passey and Henkes, 2012) predicts reaction progress equally well for temperatures and timescales relevant to sedimentary basins. We evaluate our laboratory-based rate predictions by studying brachiopod calcite from several sedimentary basins with independently constrained burial temperature histories. Specifically, we use the laboratory-derived Arrhenius parameters to predict the evolution of brachiopod calcite clumped isotope compositions during successive one million-year time steps reflecting the burial and exhumation temperature paths of each basin. While this exercise is limited by the relatively large uncertainties in the temperature histories of these basins, we find general correspondence, within error, between predicted and observed clumped isotope values. We present simplified temperature–time diagrams for calcite showing domains where primary clumped isotope compositions will be preserved, partially reordered, and fully reordered. In conclusion, calcite samples dwelling at $\sim 100^\circ\text{C}$ or lower for 10^6 – 10^8 year timescales should not be affected by solid-state C–O bond reordering.

© 2014 Elsevier Ltd. All rights reserved.

* Corresponding author. Tel.: +1 410 516 7135; fax: +1 410 516 7933.

E-mail address: ghenkes1@jhu.edu (G.A. Henkes).

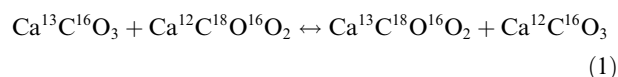
1. INTRODUCTION

Clumped isotope thermometry of fossil marine carbonates has provided new insight into the paleotemperatures and oxygen isotope compositions of ancient seawaters (Came et al., 2007; Keating-Bitonti et al., 2011; Price and Passey, 2013), revealed evidence for large global climatic shifts (e.g., the Late Ordovician–Early Silurian glaciation; Finnegan et al., 2011), and differentiated estuarine from marine paleoenvironments (e.g., in the Cretaceous Western Interior Seaway; Dennis et al., 2013). Undoubtedly, deep-time paleoceanography using the skeletons of marine organisms will continue to be a major application of this relatively new paleothermometer, in part because of the fundamental questions that can be addressed, such as the possibility of hot Early Paleozoic oceans (Joachimski et al., 2009; Finnegan et al., 2011; Grossman, 2012a), the role of cooling in Ordovician biodiversification (Sheehan, 2001; Trotter et al., 2008), and the isotopic evolution of seawater (Veizer et al., 1999; Eiler, 2011). This technique has also been applied to reconstructions of ancient terrestrial paleotemperatures and meteoric water $\delta^{18}\text{O}$ (e.g., Ghosh et al., 2006a; Passey et al., 2010). Despite the apparent success of this new method, relatively little is known about the physical conditions required for long-term ($\sim 10^6$ – 10^9 years) preservation of primary carbonate clumped isotope paleotemperatures. The goal of this study is to establish a quantitative basis for defining those conditions through analysis of fossil brachiopod shells, which have become a *de facto* standard for pre-Mesozoic stable isotope paleothermometry (Veizer et al., 1999; Grossman, 2012a).

Brachiopod shells have been the preferred material for deep-time isotopic paleotemperature studies because of their widespread occurrence in space and time, relatively large size, and stable mineralogy and chemistry (low-Mg calcite). However, preservation of shell chemistry for hundreds of millions of years has long been a concern (e.g., Land, 1995; Veizer, 1995). This has led to a variety of analytical approaches to evaluate preservation of fossil shells, including petrographic and cathodoluminescence microscopy, scanning electron microscopy, trace and minor element analysis, and X-ray powder diffraction (e.g., Compston, 1960; Popp et al., 1986; Veizer et al., 1986; Grossman et al., 1996; Mii et al., 1997). In addition, cements and replacement calcites associated with fossils have also been studied to understand isotopic and chemical trends associated with diagenesis. The net result of applying various combinations of these techniques is highly screened stable isotope records that are believed to represent conditions at the ancient Earth surface (Grossman, 2012b). All of the recent carbonate clumped isotope studies of marine fossils have used some combination of these diagenetic screening techniques (Came et al., 2007; Finnegan et al., 2011; Keating-Bitonti et al., 2011; Brand et al., 2012; Dennis et al., 2013; Price and Passey, 2013). Therefore, these clumped isotope paleotemperature records are thought to be devoid of major diagenetic imprints, at least to limits of detection for the most common screening tests.

However, clumped isotope paleotemperatures from primary carbonates are susceptible to alteration via C–O bond

reordering in the solid mineral lattice. Specifically, such ‘reordering’ must involve the breakage of existing C–O bonds, and reforming the C–O bonds with allochthonous C or O originating from, for example, neighboring carbonate groups, or interstitial positions. Such reordering is likely related to solid-state diffusion of C and O atoms through the mineral lattice. Regardless of the exact mechanism(s), the net result is a change in the abundance of ^{13}C – ^{18}O bonds (and other isotope-specific bonds), as illustrated by the following isotope exchange reaction (for the case of calcium carbonate):



This process can reset primary clumped isotope compositions without changing the texture, $^{18}\text{O}/^{16}\text{O}$, $^{13}\text{C}/^{12}\text{C}$, or trace element composition of the calcite. Because the process involves reordering of C–O bonds at the molecular to unit-cell scale, it does not require mass exchange with external fluids or gases, as would be required to alter $^{18}\text{O}/^{16}\text{O}$ and $^{13}\text{C}/^{12}\text{C}$ via self-diffusion (e.g., Anderson, 1969; Kronenberg et al., 1984; Farver, 1994). Studies of marbles and carbonatites suggest ‘closure temperatures’ for this process of approximately 150–250 °C (Dennis and Schrag, 2010). However, these closure temperatures are cooling-rate dependent (Passey and Henkes, 2012), and knowledge of the clumped isotope compositions of marbles and carbonatites does not provide a basis for accurate prediction of reordering rates at lower temperatures that might be experienced during burial and exhumation of paleoclimate archives.

The kinetics of C–O bond reordering have recently been investigated via timed heating experiments on two natural calcites (Passey and Henkes, 2012). Arrhenius parameters derived from these experiments predict that for timescales of 10^6 – 10^8 years, burial temperatures of ~ 100 – 150 °C may lead to measurable alteration of primary clumped isotope paleotemperatures. Thus, it is possible that the marine carbonate clumped isotope paleotemperature record includes data from samples that were at least partially reordered. This is problematic because unlike dissolution/reprecipitation-type diagenesis of fossil calcite, purely reordered samples are not identifiable by existing chemical and textural approaches.

In this study, we present carbonate clumped isotope results from 12 Carboniferous brachiopod shells collected from five ancient sedimentary basins now exposed in the United States and Russia. These samples are ‘well-preserved’ from the viewpoint of texture (thin sections) and bulk geochemistry (cathodoluminescence), but their clumped isotope paleotemperatures range from 35 to 165 °C, with the higher temperatures clearly pointing to alteration. We then present results of a set of laboratory heating experiments, similar to those of Passey and Henkes (2012), performed on aliquots of calcite from a Permian brachiopod shell. We evaluate these data in the context of first-order reaction progress (Passey and Henkes, 2012), as well as a new non-first-order kinetic model, and determine Arrhenius parameters that allow for prediction of reordering over temperatures and timescales relevant to sedimentary basins. Predictions based on the experimental data are evaluated

against brachiopod clumped isotope data from the five Carboniferous basins, and calcite data from the Carrara marble (a deep-burial, high-temperature end-member). Brachiopod calcite is ideal for such tests because, unlike calcite in micritic limestones or sedimentary cements, it provides constraints on primary texture, chemistry, and temperature of mineralization (probably less than 40 °C, and certainly less than 50 °C, given the current understanding of thermal limits for complex animal life; e.g., [Ravaux et al., 2013](#)). Thus, for brachiopods we have a basis for determining whether or not calcite has been extensively altered (chemically or physically), and can therefore avoid such samples in our analysis (since we are studying solid-state diffusion processes, and not recrystallization processes such as dissolution/precipitation, authigenic carbonate overgrowths or infillings of porosity, and other non-primary mineralization). Our experiments help place new constraints on the timescales and burial conditions most likely to afford preservation of original shell clumped isotope paleotemperatures.

2. CARBONIFEROUS BRACHIOPODS

We studied several pristine Carboniferous brachiopod shells from the United States and Russia ([Table 1](#)). The samples come from the Bird Spring Formation, Nevada (Early Pennsylvanian; [Jones et al., 2003](#)), the Grove Church Formation, Illinois (Late Mississippian; [Flake, 2011](#)), the Glenshaw Formation, West Virginia (Late Pennsylvanian; [Flake, 2011](#)), the Fern Glen Formation, Missouri (Early Mississippian; [Mii et al., 1999](#)) and from the Cheremchanskian and Krasnopolyanskian Horizons exposed in the Ural Mountains, Russia (Early Pennsylvanian; [Mii et al., 2001](#)). The tectonic setting of these basins include active arc-continent and continent–continent convergent margin tectonics (Nevada and the Ural Mountains, respectively), and relatively stable intra-plate basins (Illinois, West Virginia, and Missouri) with sediment supplied by adjacent mountain building resulting from convergent tectonics. The burial histories of these basins are discussed in detail in [Section 4](#).

2.1. Analytical methods

Prior to stable isotope analysis, we characterized the preservation of brachiopods using plane-polarized light and cathodoluminescence (CL) microscopy. An example of results is shown in [Fig. 1](#), and results for other specimens are provided in Electronic Annex 1 (Figs. S1–S11). Some of this screening was done by referencing previous characterizations of these specimens by [Mii et al. \(1999, 2001\)](#). New or more detailed imaging was performed at Texas A&M University using a Technosyn 8200 MKII CL stage mounted on a petrographic microscope. Based on these images, each shell was assigned a qualitative CL character ([Table 1](#)). Non-luminescent (NL) and semi-luminescent (SL) shells are considered pristine and near-pristine, respectively, whereas luminescent shells reflect uptake of trace elements (primarily Mn) and hence are not considered in this study. The prismatic secondary or tertiary shell layers were sampled, with care taken to avoid material from the primary shell layer, which is commonly observed to be

recrystallized (e.g., [Adlis et al., 1998](#)) and exhibit vital effects (e.g., [Carpenter and Lohmann, 1995](#)).

Stable isotope compositions of the fossil shells and their associated limestone matrices were determined at Johns Hopkins University (JHU) using methods described in [Henkes et al. \(2013\)](#). Carbonate clumped isotope compositions are expressed in Δ notation:

$$\Delta_{47} = \left[\left(\frac{R^{47}}{R^{47*}} - 1 \right) - \left(\frac{R^{46}}{R^{46*}} - 1 \right) - \left(\frac{R^{45}}{R^{45*}} - 1 \right) \right] \times 1000 \quad (2)$$

where R^i = mass i /mass 44 and the asterisk indicates ratios for isotopologues at stochastic abundance levels ([Affek and Eiler, 2006](#)). Mass 47 CO₂ contains the ¹³C–¹⁸O bond on which the thermometer is based ([Ghosh et al., 2006b](#)). Oxygen and carbon isotope values are expressed in δ notation, on either the VPDB (mineral) or VSMOW (water) scales.

All carbonate clumped isotope values in this study are presented on an absolute reference frame, herein referred to as the ‘carbon dioxide equilibrium scale’ or CDES, which empirically corrects for instrumental nonlinearities and changes in the ionization environment during mass spectrometry ([Dennis et al., 2011](#)). This reference frame was established by periodically analyzing aliquots of CO₂ that were isotopically equilibrated at 30 or 1000 °C (for details see [Henkes et al., 2013](#)). We analyzed at least one of these equilibrium CO₂ reference gases every 1–2 days, thus cycling through four isotopically distinct gases weekly or sub-weekly.

The international standard NBS-19 and two internal carbonate standards, UU-Carrara and 102-GC-AZ01, were regularly analyzed alongside samples to monitor system stability and precision, with the following long-term averages: NBS-19 ($n = 9$) $\Delta_{47} = 0.404 \pm 0.009\text{‰}$ (CDES, mean $\pm 1\sigma$ standard deviation); UU-Carrara ($n = 27$) $\Delta_{47} = 0.402 \pm 0.017\text{‰}$; 102-GC-AZ01 ($n = 36$) $\Delta_{47} = 0.713 \pm 0.012\text{‰}$. The $\delta^{13}\text{C}$ and $\delta^{18}\text{O}$ values of samples were corrected using concurrent analyses of NBS-19. An effort was made to analyze each sample in triplicate during different analytical sessions to minimize session-specific bias, although for some samples replicate measurements were made during a single session ([Table S1](#)).

Temperatures were calculated from Δ_{47} using the theoretical Δ_{47} -temperature relationship from [Schauble et al. \(2006\)](#), adjusted for the kinetic effects of calcite phosphoric acid digestion ([Guo et al., 2009](#)). The theoretical Δ_{47} temperature calibration was used because of the lack of empirical calibrations in the range of temperatures corresponding to the Carboniferous brachiopod clumped isotope compositions (up to ~150 °C) and our experimental temperatures. For brachiopod samples thought to have retained their primary clumped isotope compositions, we used the modern mollusk and brachiopod temperature calibration from [Henkes et al. \(2013\)](#) to calculate paleotemperatures.

2.2. Results for Carboniferous brachiopods and associated cements

Carbonate clumped isotope paleotemperatures ($T(\Delta_{47})$) of fossil brachiopod shells ranged from 20 ± 5 °C to

Table 1

Stable isotope compositions of Carboniferous brachiopods from North America and Western Russia.

Sample ID	Taxonomic information	CL Character	n	$\delta^{13}\text{C}_\text{c}$ (‰ VPDB)	$\delta^{18}\text{O}_\text{c}$ (‰ VPDB)	Δ_{47} (‰ CDES) ^a	T(Δ_{47}) (°C) ^b	$\delta^{18}\text{O}_\text{w}$ (‰ VSMOW) ^c
North America								
<i>Fern Glen Formation (upper Mississippi Valley, Missouri, USA), Early Mississippian (348–340 Ma)</i>								
MO074	<i>Prospira vernonensis</i>	NL	3	3.60 ± 0.36	−1.93 ± 0.14	0.708 ± 0.013	20 ± 5	−1.5
MO076	<i>Prospira vernonensis</i>	NL	3	3.16 ± 0.05	−1.75 ± 0.05	0.686 ± 0.016	29 ± 7	0.6
MO077	<i>Prospira vernonensis</i>	NL/SL	3	4.14 ± 0.08	−1.97 ± 0.07	0.695 ± 0.011	25 ± 4	−0.4
<i>Bird Spring Formation (eastern Great Basin province, Nevada, USA), Late Mississippian (323 Ma)</i>								
NV007	productid	NL	3	2.66 ± 0.05	−1.06 ± 0.04	0.439 ± 0.012	157 ± 12	17.2
NV008	productid	NL/SL	3	2.84 ± 0.03	−1.04 ± 0.03	0.430 ± 0.013	166 ± 13	17.8
NV014	productid	NL	3	1.55 ± 0.04	−0.78 ± 0.07	0.448 ± 0.005	148 ± 4	16.9
NV021	<i>Anthracospirifer</i>	NL/SL	3	2.32 ± 0.04	−0.40 ± 0.04	0.461 ± 0.013	137 ± 11	16.4
<i>Grove Church Formation (southern Illinois Basin, Illinois, USA), Late Mississippian (333–318 Ma)</i>								
WP58 Inf-1	<i>Inflatia</i>	NL	3	1.26 ± 0.03	−3.33 ± 0.03	0.621 ± 0.004	48 ± 2	2.4
<i>Glenshaw Formation (Appalachian Basin, West Virginia, USA), Late Pennsylvanian (305–299 Ma)</i>								
WP50b NS-1	<i>Neospirifer</i>	NL/SL	3	2.72 ± 0.03	−3.66 ± 0.06	0.652 ± 0.002	35 ± 1	−0.3
WP53 NS-1	<i>Neospirifer</i>	NL/SL	3	1.92 ± 0.03	−3.70 ± 0.05	0.633 ± 0.008	42 ± 4	1.1
Western Russia								
<i>Cheremchanskian & Krasnopolyanskian Horizons (Urals Mountains, Russia), Early Pennsylvanian (318 Ma)</i>								
RU124	<i>Choristites</i>	NL	3	4.84 ± 0.02	−1.02 ± 0.18	0.448 ± 0.016	149 ± 14	16.6
RU129A	<i>Choristites</i>	NL	3	4.66 ± 0.06	−2.48 ± 0.11	0.450 ± 0.015	147 ± 13	15.0

Note: Error values are standard error of the mean ($= \pm 1\sigma/\sqrt{n}$), where 1σ is the standard deviation of n analyses. When $n = 2$ the error value is 1σ (standard deviation).

^a Values relative to the ‘carbon dioxide equilibrium scale’ or CDES. An acid correction factor of 0.092‰ was applied to normalize these data to the 25 °C phosphoric acid reaction scale.

^b Paleotemperatures calculated using linear regressions through the theoretical Δ_{47} -temperature relationship from Schauble et al. (2006) adjusted for the kinetic effects of calcite phosphoric acid reaction (Guo et al., 2009). A regression of model predictions from 0 to 50 °C ($\Delta_{47} = 38,455/T^2 + 0.258$) was used for ‘WP’ samples and a regression from 50–250 °C ($\Delta_{47} = 41,746/T^2 + 0.213$) was used for ‘NV’ and ‘RU’ samples. The modern calibration from Henkes et al. (2013) was used for ‘MO’ samples. Error was calculated by propagating the analytical error for Δ_{47} through these linear equations.

^c Water isotope compositions calculated using clumped isotope derived paleotemperatures and the calcite oxygen isotope thermometry equation of O’Neil et al. (1969): $1000\ln\alpha = 2.78 \times 10^6/T^2 - 3.39$ for temperatures > 50 °C. For temperature < 50 °C the equation of Kim and O’Neil (1997): $1000\ln\alpha = 18.03 \times 10^3/T - 32.42$ was used.

166 ± 13 °C (Fig. 2, Table 1, EA 2). The higher temperatures are clearly incompatible with shell growth, whereas the lower temperatures seem plausible for the low-paleolatitude tropical seas from which they originated (Mii et al., 1999, 2001). Measured brachiopod shell $\delta^{18}\text{O}$ values were used with T(Δ_{47}) to solve calcite–water oxygen isotope thermometry equations (e.g., O’Neil et al., 1969 and Kim and O’Neil, 1997) for the oxygen isotope composition of the waters ($\delta^{18}\text{O}_\text{w}$) that would have been in equilibrium with these shells. Calculated $\delta^{18}\text{O}_\text{w}$ values ranged from −0.4‰ to 17.8‰ (Table 1). Again, the higher-end values in this range are incompatible with primary shell growth in ancient seawater. Note that the data in Fig. 2 generally plot along ‘closed-system pathways’ defined by solutions to the calcite–water $\delta^{18}\text{O}$ thermometry equations for constant calcite $\delta^{18}\text{O}$. In other words, the drastically altered clumped isotope compositions are not accompanied by obvious changes in calcite $\delta^{18}\text{O}$, a pattern consistent with solid-state reordering or low water/rock ratio recrystallization. The most extreme examples of this behavior are brachiopods from Arrow Canyon, NV, USA and the Ural Mountains in Russia (Fig. 2). Associated carbonate matrix from Arrow Canyon and the Ural Mountains (Fig. S12, Table S2) have T(Δ_{47}) values that range from 89 to 127 °C, which are

cooler than each of the associated brachiopods, but warmer than expected for early diagenetic cements.

The T(Δ_{47}) data in Fig. 2 pose a problem: How can primary paleotemperatures be identified when analyses of brachiopods of similar textural and chemical preservation yield a ~150 °C apparent temperature range? Given the elevated clumped isotope temperatures, the lack of evidence for extensive recrystallization, and the apparently primary calcite $\delta^{18}\text{O}$ values we conclude that much of this temperature range results from solid-state reordering of C–O bonds at elevated burial temperatures experienced by some of these samples. An understanding of the temperatures and timescales over which such reordering becomes important will aid in identification of sedimentary strata and fossils most capable of preserving primary clumped isotope compositions.

3. EXPERIMENTAL DETERMINATION OF REORDERING KINETICS IN BRACHIOPOD CALCITE

3.1. Experimental methods and observations

Timed heating experiments were conducted on a fossil brachiopod shell fragment (WA-CB-13) collected from the

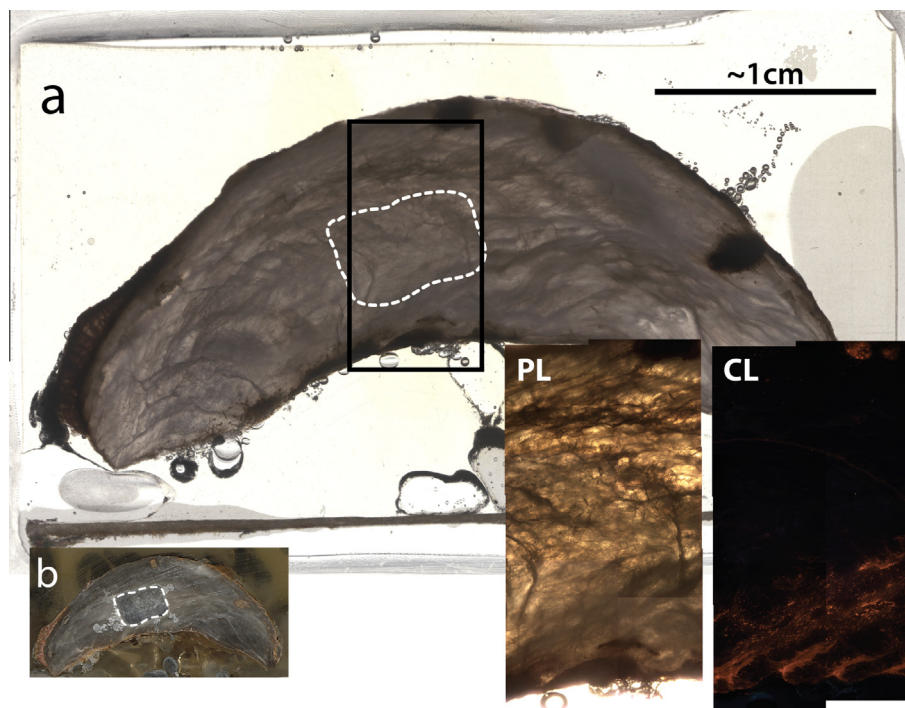


Fig. 1. Scanned sample thin section (a) and billet (b), and plane-light (PL) and cathodoluminescence (CL) photomicrograph mosaics for a Carboniferous productid brachiopod (NV007) from the Bird Spring Formation, Arrow Canyon, NV, USA. The black box in (a) corresponds to the area covered by the photomicrograph images. This sample represents a typical nonluminescent (NL) brachiopod shell (Table 1). The sample billet (b) was scanned after sub-sampling from the area inside the white dashed line (also shown in 1a).

Lower Permian Callytharra Formation in the Carnarvon Basin of Western Australia (Sakmarian-Artinskian Stage, ~290 mya). This formation contains the oldest Permian sediments in the region free of Late Paleozoic glacial influence (Dixon and Haig, 2004; Mory and Haig, 2011). This shell was selected over the lower-temperature Carboniferous shells shown in Fig. 2 because of the large sample size requirements (see below) for heating experiments run at several temperatures. The design of the heating experiments closely follows the methods of Passey and Henkes (2012). The shell fragment ($3.4 \times 2.4 \times 0.8$ cm) was crushed in a mortar and pestle and sieved through 125 and 251 μm mesh. This size fraction was then rinsed and ultrasonicated in deionized water to remove smaller adhered particles. The cleaned material was dried at 60 °C for 24 h and stored in a desiccator. Approximately 30 mg aliquots of the crushed shell material were loaded into fused silica tubes, dried *in vacuo* at 100 °C for 1 h, and then torch-sealed along with ~80 μmol of dry CO_2 . The isotopic composition of the CO_2 was $\delta^{13}\text{C} = -39\text{‰}$ (VPDB) and $\delta^{18}\text{O} = -31\text{‰}$ (VPDB), which was significantly different than the shell ($\delta^{13}\text{C} = 3.75\text{‰}$; $\delta^{18}\text{O} = -0.66\text{‰}$), allowing for monitoring of isotopic exchange between the mineral and CO_2 as might result from unintended dissolution/precipitation reactions.

The silica tubes containing aliquots of WA-CB-13 were held at temperatures ranging from 385–475 °C inside tube furnaces for time periods of 30 min to 4 days. Each tube was quickly removed from the furnace at prescribed intervals and quenched to room temperature (<30 s) with compressed air. Calibration curves between thermocouple-

indicated furnace temperature and actual temperature were generated regularly by observation of *in vacuo* melting points for Sn, Zn, and Al using their ITS 90 reference values (Preston-Thomas, 1990), and the uncertainty in absolute temperature was less than 3 °C.

The average Δ_{47} value of unreacted shell material was $0.669 \pm 0.010\text{‰}$ (CDES), which corresponds to a growth temperature of 37 ± 5 °C (using the mollusk- and brachiopod-specific calibration reported by Henkes et al., 2013). Electron microprobe analyses of unreacted and reacted WA-CB-13 grains revealed low Mn and Fe contents (128–216 $\mu\text{mol/mol}$ Mn/Ca, 36–110 $\mu\text{mol/mol}$ Fe/Ca; Table S3), suggesting that the shell fragment did not undergo obvious natural meteoric diagenesis, and did not change in minor element composition during experimental heating (Popp et al., 1986). Heated grains of WA-CB-13 appeared similar to unheated grains in terms of size, shape, surface luster, and color. However, in some longer experiments, a slight darkening of the grains was observed. This may have been caused by pyrolyzation of trace amounts of organic carbon, or reduction of calcite to graphite, or calcite decomposition, and is similar to observations for heated optical and spar calcite studied by Passey and Henkes (2012).

In several reactions at 425–475 °C, a small amount of condensation was observed on the inside of the silica tubes following the quench to room temperature (noted in Table S4). The source of this fluid is unknown, but it is possible that it came from decrepitation of fluid inclusions or hydrolysis of organic carbon occluded in the shells. Of relevance as to whether the presence of such water might affect

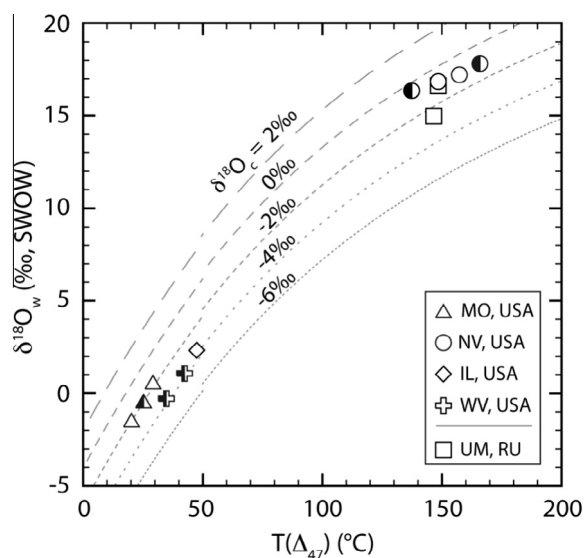


Fig. 2. Carboniferous brachiopod carbonate clumped isotope temperatures ($T(\Delta_{47})$) versus apparent water oxygen isotope compositions of the precipitating waters ($\delta^{18}\text{O}_w$). Water oxygen isotope values were determined from measured carbonate $\delta^{18}\text{O}$ and $T(\Delta_{47})$ using the calcite–water oxygen isotope thermometry equation of Kim and O’Neil (1997). For paleotemperatures greater than 50 °C, the equation of O’Neil et al. (1969) was used. Details on the Δ_{47} –temperature relationships used to determine the temperatures are in Table 1. Open symbols represent non-luminescent (NL) shells, whereas half-filled symbols represent semi-luminescent (SL) shells. The gray dashed and dotted lines represent solutions to the calcite–water oxygen isotope thermometry equations for constant carbonate $\delta^{18}\text{O}_c$ values, as noted above the figure.

reordering rates, Passey and Henkes (2012) conducted both dry (CO_2 , ~0.1 MPa) and wet (H_2O , ~0.1 and ~100 MPa) reordering experiments on calcite at 425 °C, and observed no difference in reordering rates between these treatments. Thus we do not expect this fluid to have a large influence on the reordering behavior of our current experiments. As discussed in Passey and Henkes (2012), the apparent insensitivity of clumped isotope reordering rates on $f_{\text{H}_2\text{O}}$ is consistent with recent evidence (Labotka et al., 2011) that the mechanism of increased apparent rates of O diffusion in calcite at elevated $f_{\text{H}_2\text{O}}$ relates to reactions between water and calcite at the mineral surface, and not to changes in the diffusivity of the bulk mineral.

However, we did observe systematic 0.2–0.4‰ decreases in $\delta^{18}\text{O}$ of reacted samples (Table S4), and we also observed that the samples did not approach equilibrium Δ_{47} values as closely as was observed in previous experiments with optical calcite (Passey and Henkes, 2012). Complete oxygen isotope exchange between CO_2 and calcite in our experiments would result in a lowering of the calcite $\delta^{18}\text{O}$ by about 6‰ (calculated using CO_2 –calcite fractionation factors from Chacko et al., 1991), and hence an observed change of 0.3‰ represents an approach to equilibrium of about 5%. At the same time, we observed no change in $\delta^{13}\text{C}$ values of reacted samples, despite an equilibrium value for complete C exchange between CO_2 and calcite about 10‰ lower than the initial composition of the mineral. These findings

suggest that the observed change in $\delta^{18}\text{O}$ probably does not reflect dissolution and reprecipitation of mineral lattice (which we expect would result in decreases of mineral $\delta^{13}\text{C}$ values). Perhaps the change in $\delta^{18}\text{O}$ is a result of solid-state O diffusion (which is significantly faster than C diffusion; e.g., Labotka et al., 2011), or some intrinsic change in the acid fractionation factor related to dewatering of the samples, or other unknown factors. With this caveat, we proceed with interpreting the observed clumped isotope changes as reflecting solid-state reordering only.

3.2. Heating experiment isotopic results

The isotopic compositions ($\delta^{13}\text{C}$, $\delta^{18}\text{O}$, and Δ_{47}) of our heating experiment samples are presented in Table S4 and illustrated (Δ_{47} only) in Figs. 3a–c. For comparison, we plot these data alongside results for optical calcite (Fig. 3d–f) from Passey and Henkes (2012). These two materials show similar Δ_{47} changes with time, including (1) progressive decrease throughout the reaction, (2) higher rates of decline at higher temperature, (3) an initial, rapid decline followed by a less rapid decrease after several hundred minutes, and (4) an asymptotic approach towards high temperature equilibrium Δ_{47} values of 0.30–0.35‰ for higher temperature reactions. Fig. 3b and e plot the data in terms of first-order reaction progress (Passey and Henkes, 2012):

$$\ln(1 - F) = -kt = \ln \left[\frac{\Delta_{47}^t - \Delta_{47}^{eq}}{\Delta_{47}^{init} - \Delta_{47}^{eq}} \right] \quad (3)$$

where Δ_{47}^t is the value of the sample at a time duration t , and Δ_{47}^{init} and Δ_{47}^{eq} are the initial and equilibrium Δ_{47} values, respectively, F is the fractional approach to equilibrium, and k is the reaction rate constant. The temperature-dependent Δ_{47}^{eq} values used in this study are the same as reported by Passey and Henkes (2012), but adjusted by +0.011‰ to account for the difference in acid fractionation factors used in this study (0.092‰; see Henkes et al., 2013) versus the previous study (0.081‰). Fig. 3b and e clearly show that the reaction is not strictly first-order since the data for a given reaction temperature do not plot along straight lines (except for data from samples closely approaching equilibrium), and do not have intercepts at the origin. Instead, the data show early, rapid reordering followed by slower reordering.

3.3. Carbonate clumped isotope reordering models

We consider two alternative kinetic models for the data. The first model treats the data in terms of first-order kinetics (‘first-order approximation’ model; Passey and Henkes, 2012), whereas the second, a new ‘transient defect/equilibrium defect’ model, accounts for all parts of the reaction progress curve. Both models are based on the hypothesis that crystallographic defects, particularly point defects, are the vehicle by which solid-state diffusion occurs (Lasaga, 1998; Cole and Chakraborty, 2001; Kittel, 2005; Zhang, 2010). Defects can be classified as intrinsic, extrinsic, or ‘structural’. Intrinsic defects have concentrations that are a function of temperature and exist as a consequence of the thermodynamic battle between order and

energy. In contrast, extrinsic defects arise from ionic impurities with radii and charges similar to or different from those of native ions, as well as other non-intrinsic point defects generated during crystal growth. Lastly, structural defects are those associated with dislocations, low and high angle grain boundaries, surfaces, radiation damage zones, and macroscale inclusions. For example, a Frenkel defect is a type of intrinsic defect consisting of a vacancy-interstitial pair created by migration of an atom from a lattice position to an interstitial position. The number of Frenkel defects increases with temperature according to $n \cong N \exp(-E_p/2k_B T)$ where N is the total number of atoms, E_p is the energy required to create a vacancy-interstitial pair, k_B is Boltzmann's constant, and T is temperature in Kelvin (Kittel, 2005). Of these defect types, intrinsic defects can be considered to be 'unannealable': their concentrations are not reduced or changed during prolonged heating at elevated temperature (but note that with the onset of heating, the concentration of intrinsic defects will adjust to the new thermodynamic equilibrium). In contrast, certain types of extrinsic and structural defects are 'annealable': prolonged heating can act to eliminate ('annihilate' or 'heal') or otherwise immobilize these defects (i.e., the defect becomes fixed in its spatial coordinate and is no longer able to effect C–O bond reordering). The models presented below are based on the dichotomy of annealable defects, here termed 'transient' defects, and unannealable defects, here termed 'equilibrium' defects. Note that the latter is not strictly limited to intrinsic defects; for example, it is generally not possible to remove ionic impurities simply by heating samples under closed-system conditions.

3.3.1. First-order approximation model

As described in Passey and Henkes (2012), this model assumes that the initial rapid reaction observed in our experiments (first several hundred minutes; Fig. 3a and c) is influenced by 'transient' defects. The existence of annealable defects in calcite and their promotion of rapid rates of solid-state diffusion have previously been observed in studies of O self-diffusion in calcite (Kronenberg et al., 1984; Farver, 1994), although the nature of these defects has not been resolved. We further define a transient defect as any defect whose role in promoting C–O bond reordering is deactivated by prolonged heating. The transient defects are deactivated early in the experiment after effecting a finite amount of ^{13}C – ^{18}O reordering, while equilibrium defects persist indefinitely, with constant, temperature-dependent concentrations. Thus, equilibrium defects give rise to the first-order reaction progress observed during the latter part of the reactions (see Passey and Henkes, 2012, for further justification for applying first-order rate laws to ^{13}C – ^{18}O bond reordering).

For determination of first-order rate constant regressions and Arrhenius parameters (Fig. 3c and f) we will exclude the early transient defect-related data (unfilled data in Fig. 3b and e) from consideration. The justification for this exclusion is given by Passey and Henkes (2012), who argue that transient defects anneal early in the thermal evolution of carbonates previously residing at high temperatures (e.g., marbles and carbonatites). The general purpose

of the present study, however, is to constrain reordering rates at elevated temperatures for samples initially residing at surface temperatures. Therefore, we cannot assume that transient defects have been annealed, and we must make the assumption that the annealable defects are mostly inactive (in terms of effecting C–O bond reordering) at temperatures relevant to burial of paleoclimate archives ($\sim 200^\circ\text{C}$ or lower). This assumption is evaluated in our development of the extended 'transient defect/equilibrium defect' model (Section 3.3.2), and indirectly in Section 4, where we compare predicted clumped isotope compositions of Carboniferous brachiopods (based on the Arrhenius parameters applied to known burial temperature histories) to measured clumped isotope compositions.

The slope of linear regressions through the data exhibiting apparent first-order behavior (filled symbols in Fig. 3b and e) provide values for the reaction rate constant k (Fig. 3b, Table 2). Appendix B discusses the criteria used to include or exclude data from rate constant regressions; in short, the included data are from reaction durations longer than the period in which the transient reordering is active, but shorter than the period when clumped isotope compositions closely approach their equilibrium values.

According to the Arrhenius relation:

$$k = K_0 e^{\left(\frac{-E_a}{RT}\right)} \quad (4)$$

where K_0 is a constant referred to as the frequency factor. A plot of $\ln(k)$ versus $1/T$ for each experiment will have a slope of $-E_a/R$, where E_a is the activation energy and R is the universal gas constant, and an intercept of $\ln(K_0)$ (Fig. 3c and f). The Arrhenius parameters for WA-CB-13 are presented in Table 2, along with the data and calculated Arrhenius parameters for the optical calcite (MGB-CC-1, from Passey and Henkes, 2012). We find that the activation energies of the brachiopod calcite and the optical calcite are identical within error, and that their frequency factors are marginally distinguishable. Note that for two experimental temperatures for WA-CB-13, only two points are used for the Arrhenius regressions (Table 2). This was unavoidable given the criteria used for selecting points to define the equilibrium defect behavior (Appendix B) and the lack of sufficient sample for additional experiments.

3.3.2. Transient defect/equilibrium defect model

This model, developed fully in Appendix A, accounts for C–O bond reordering due to both transient defects and equilibrium defects. The first step in this analysis is to quantify the reordering kinetics due to equilibrium defects, which is procedurally and mathematically equivalent to quantifying rate constants in the 'first-order approximation' model discussed above, and hence yields the same Arrhenius parameters. We then mathematically subtract the influence of the equilibrium defect pool on the overall reaction progress, leaving a reaction progress that is solely attributable to transient defects (the 'curve-stripping' procedure is described in Appendix B). The resulting reaction progress is non-first-order, reflecting the fact that the rate constant is a function both of defect concentration and the efficacy of those defects at promoting C–O reordering. Since the concentration of transient defects decreases with

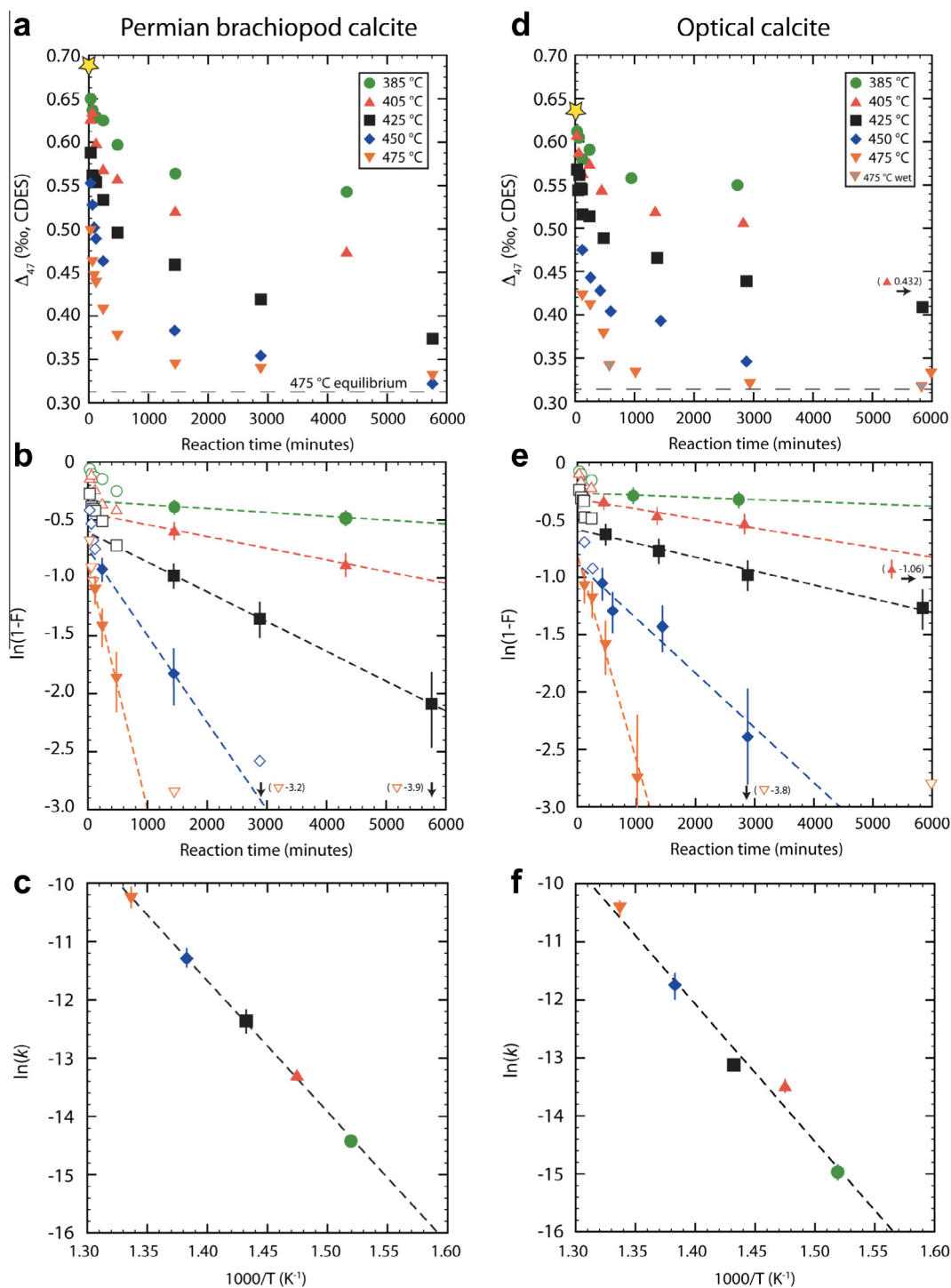


Fig. 3. Results of the reordering experiments on the Permian brachiopod shell WA-CB-13, and for comparison the results of analogous experiments performed on an optical calcite, MGB-CC-1, from [Passey and Henkes \(2012\)](#). (a, d) Measured Δ_{47} values as a function of time. The temperatures of each heating experiment are indicated in the legend. The yellow stars denote the initial compositions of the materials and the dashed line marks the theoretical equilibrium value for 475 °C, shifted by +0.092‰ to account for the acid fractionation for 90 °C reactions ([Henkes et al., 2013](#)). (b, e) Reordering reaction progress, plotted as $\ln(1 - F)$, as a function of time. The dashed lines represent best-fit linear regressions to the data identified as having first-order behavior, whose slopes are equivalent to the reaction rate constant k (Eq. (3), [Table 2](#)). Unfilled symbols at times <1000 min correspond to non-first-order reaction and thus are not included in the linear regressions. Unfilled symbols at times >1000 min correspond to data that closely approach equilibrium for the respective reaction temperatures and are also not included in the linear regressions (see [Appendix A](#)). (c, f) Arrhenius plots for determining the activation energies (E_a) and frequency factors (K_0) for the first-order approximation model. The slopes of the regressions equal $-E_a/R$, where R is the universal gas constant, and the intercepts equal $\ln(K_0)$.

Table 2

Rate constant regressions and Arrhenius parameters for the first-order approximation model for Permian brachiopod calcite WA-CB-13 and an optical calcite from [Passey and Henkes \(2012\)](#), for comparison.

Reaction T (°C)	Slope (=−k) (s ^{−1})	Intercept	R ²	SRX points used ^a
<i>WA-CB-13</i>				
385	-5.52×10^{-7}	−0.34	—	037, 042
405	-1.68×10^{-6}	−0.44	0.98	033, 041, 044
425	-4.29×10^{-6}	−0.61	1.00	012, 013, 014
450	-1.25×10^{-5}	−0.75	—	020, 031
475	-3.50×10^{-5}	−0.88	1.00	017, 021, 029
Arrhenius parameters: $E_a = 188 \pm 6$ kJ/mol, $K_o = 4.45 \times 10^8 [(+27.14/-1.05) \times 10^9] \text{ s}^{-1}$				
Reaction T (°C)	Slope (=−k) (s ^{−1})	Intercept	R ²	‘RDX’ points used
<i>MGB-CC-1</i> (from Passey and Henkes, 2012)				
385	-3.18×10^{-7}	−0.27	—	181, 189
405	-1.39×10^{-6}	−0.32	0.99	169, 173, 177
425	-2.01×10^{-6}	−0.59	0.97	149, 150, 151, 153
450	-7.95×10^{-6}	−0.88	0.91	144, 145, 147, 148
475	-2.98×10^{-5}	−0.79	0.97	112, 113, 114, 115
Arrhenius parameters: $E_a = 197 \pm 19$ kJ/mol, $K_o = 1.39 \times 10^9 [(+36.0/-1.34) \times 10^9] \text{ s}^{-1}$				

Note: Regressions are best-fit, least-squares regressions calculated using the statistical software package JMP.

^a Isotope data provided in [Table S4](#).

time, the rate “constant” k is not actually constant. We therefore model k as a function of time (elapsed since initiation of heating), and for simplicity assume that the concentration of defects decreases proportional to the number of defects (a first-order rate law). The integrated rate equation for this model is ([Appendix A](#)):

$$\ln \left(\frac{\Delta_{47}^t - \Delta_{47}^{\text{eq}}}{\Delta_{47}^{\text{init}} - \Delta_{47}^{\text{eq}}} \right) = -k_c t + \frac{k_d}{k_2} (e^{-k_2 t} - 1) \quad (5)$$

Note that this equation features three rate constants, and hence three Arrhenius equations. The constant k_c is identical to the first-order rate constant in the first-order approximation model (Section 3.3.1), and describes the reordering behavior due to equilibrium defects. The constant k_d describes the efficacy of transient defects at effecting reordering, whereas the constant k_2 describes the rate at which these defects are annealed (the time-evolving concentration of defects). Regressions for determining these constants for WA-CB-13, and their Arrhenius parameters, are given in [Table B1](#). The results of these regressions for the optical calcite from [Passey and Henkes \(2012\)](#) are also given in [Table B2](#).

3.4. General predictions of the models

In this section we evaluate the extent of ¹³C–¹⁸O reordering predicted by each model as a function of time and temperature. For the first-order approximation model, Eqs. (3) and (4) can be combined, resulting in the following relationship:

$$\ln \left[\frac{\Delta_{47}^t - \Delta_{47}^{\text{eq}}}{\Delta_{47}^{\text{init}} - \Delta_{47}^{\text{eq}}} \right] = -tK_0 \exp \left[\frac{-E_a}{RT} \right] \quad (6)$$

This equation allows the prediction of reaction progress (i.e., the change in Δ_{47}) as a function of temperature T , time spent at that temperature t , and the mineral- and material-

specific Arrhenius parameters E_a and K_o . The solid lines in [Fig. 4](#) show equation (6) evaluated over a wide range of temperatures and time durations for the Arrhenius parameters of brachiopod calcite (WA-CB-13, [Fig. 4a](#)) and optical calcite (MGB-CC-1, [Fig. 4b](#)). Lines are given for T - t combinations that would result in 1% approach to isotopic equilibrium (minimal reordering) and 99% approach to isotopic equilibrium (nearly complete reordering). This figure predicts that solid-state reordering will be negligible for samples held at ~ 100 °C or lower for $\sim 10^8$ year timescales. The close correspondence between the lines for brachiopod calcite and optical calcite reflects the similarity in Arrhenius parameters observed for these materials.

For the transient defect/equilibrium defect model, equation 5 can be combined with Arrhenius equations for each of the three rate constants (i.e., as Eq. (4)) to give an equation analogous to Eq. (6) allowing prediction of reaction progress as a function of temperature and time:

$$\ln \left(\frac{\Delta_{47}^t - \Delta_{47}^{\text{eq}}}{\Delta_{47}^{\text{init}} - \Delta_{47}^{\text{eq}}} \right) = -tK_c \exp(E_c/RT) + \frac{K_d \exp(E_d/RT)}{K_2 \exp(E_2/RT)} \{ \exp[-tK_2 \exp(E_2/RT)] - 1 \} \quad (7)$$

where K_c , E_c ; K_d , E_d ; and K_2 , E_2 are the frequency factors and activation energies for the equilibrium defect component (c), transient defect component (d), and rate of annealing of the transient defect component (2). The temperature–time predictions from this model are shown as dashed lines in [Fig. 4](#). A key finding illustrated by this figure is that reordering rates are nearly identical to those predicted by the first-order approximation model for temperatures below 150–200 °C. Thus, the transient defects are inefficient at effecting C–O bond reordering at temperatures below this range, and hence are predicted to be important only for samples experiencing higher burial temperatures.

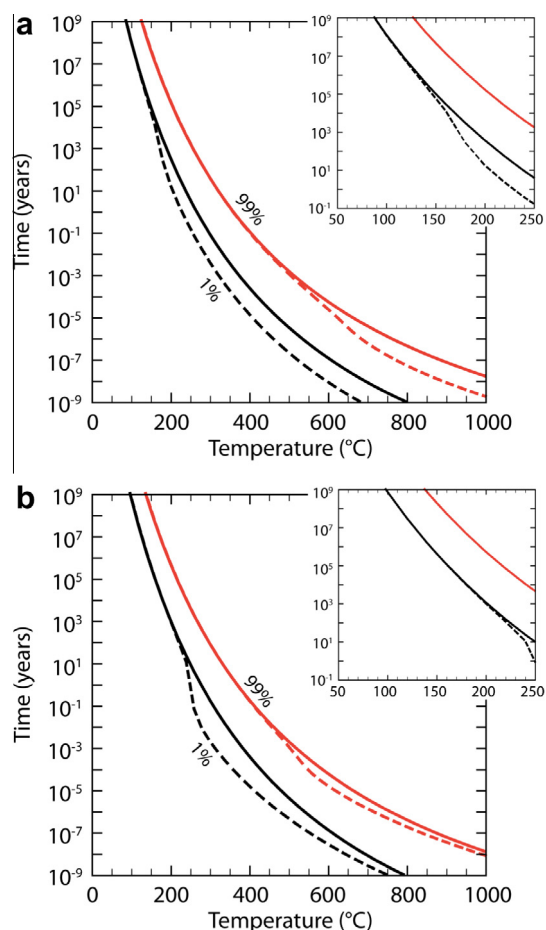


Fig. 4. Temperature-time predictions for incipient (1%) and near-complete (99%) reordering calculated using Arrhenius parameters for (a) WA-CB-13, well-preserved Permian brachiopod calcite, and (b) MGB-CC-1, an optical calcite (Passey and Henkes, 2012). The lower, black lines correspond to 1% reordering and the upper, red lines correspond to 99% reordering. The region to the left of these curves are the conditions necessary for preservation of primary carbonate clumped isotope compositions from brachiopods. The dashed lines show the ‘transient defect/equilibrium defect’ model and the solid lines show the ‘first-order approximation’ model. The inset figures focus on the conditions relevant to sedimentary burial and demonstrate that below temperatures of ~ 150 °C both models have similar behavior. (For interpretation of the references to colour in this figure legend, the reader is referred to the web version of this article.)

Geologically relevant temperature–time combinations for incipient and near-complete reordering as predicted by both of the models are listed in Table 3.

4. EVALUATION USING THE GEOLOGICAL RECORD

4.1. General approach and limitations

In this section we evaluate the laboratory-derived reordering kinetics against our observations from the geological record (Section 2). Our approach is straightforward:

we examine sedimentary strata that have reasonably good independent constraints on thermal history (e.g., from the study of fluid inclusions, conodont color alteration index, vitrinite reflectance, overburden reconstruction, and low-temperature thermochronology). For each Carboniferous basin we construct a thermal history that begins at the time of deposition, proceeds to maximum burial and through exhumation, and ends with the sample residing in outcrop at the present day. We divide the thermal history into uniform time-steps, typically one million years, which we find to be sufficiently short for accurate modeling of reordering progress. For each time-step, we use Eq. (6) to predict the extent of solid state C–O reordering that would be experienced by brachiopod calcite. This allows calculation of a new calcite Δ_{47} value that can be used as the $\Delta_{47}^{\text{init}}$ value in the next time-step of the model (this approach is functionally equivalent to using equation 13 of Passey and Henkes, 2012). We model changes in brachiopod Δ_{47} at million year time-steps, and the final result is a prediction of the final Δ_{47} value of the brachiopod after the final step (after exposure at the surface). We then compare this modeled Δ_{47} value (or equivalent $T(\Delta_{47})$) with the measured Δ_{47} values (or equivalent $T(\Delta_{47})$) of the brachiopod(s) collected from the same basin. If our laboratory-derived kinetics are valid for geological temperatures and timescales and if the burial temperature reconstructions are correct, then we should observe general correspondence between modeled and measured Δ_{47} values.

The main limitation of this approach is gaps or uncertainties in the thermal histories of the basins. As will be seen below, for many basins these uncertainties lead to large differences in the extents of predicted ^{13}C – ^{18}O reordering, in some cases ranging from no reordering to ‘complete’ reordering. As yet we have no remedy for this problem, but point out that other simple geological heating events such as contact metamorphism from emplacement of dikes and sills also have wide error margins due to uncertainties in the thermal properties of magmas and rocks and the nature of heat transfer (e.g., conductive versus convective). Despite these uncertainties, we can still examine whether laboratory-derived rate predictions are consistent with observations from the geological record. Also, we can in part work around these uncertainties by studying several basins that collectively have a wide range of thermal histories, from shallow burial of no more than ~ 1 km (mid-continental U.S.) to burial in a metamorphic core (Carrara marble).

Additionally, an irony exists in that we are treating methods like conodont color alteration, vitrinite reflectance, and fission-track annealing as yielding “correct” thermal history estimates against which our estimates of C–O reordering kinetics can be tested, whereas these burial temperature proxies arguably have more complicated and uncertain kinetics than solid-state C–O bond reordering (e.g., Castaño and Sparks, 1974; Epstein et al., 1977; Donelick et al., 2005). For example, no simple chemical reactions can be written to describe the processes of conodont color alteration or bitumen maturation. These processes undoubtedly involve vast suites of high molecular weight organic molecules, and in the case of vitrinite reflectance may also involve physical changes such as

Table 3

Temperature–time combinations for incipient (1%) and near-complete (99%) carbonate clumped isotope reordering calculated using Arrhenius parameters for Permian brachiopod calcite (WA-CB-13) and optical calcite (MGB-CC-1).

Time	Permian brachiopod calcite				Optical calcite			
	First-order approx. model		Transient defect/equil. defect model		First-order approx. model		Transient defect/equil. defect model	
	1% (°C)	99% (°C)	1% (°C)	99% (°C)	1% (°C)	99% (°C)	1% (°C)	99% (°C)
1 Ga	88	127	87	127	98	138	98	138
100 Ma	102	144	101	144	112	155	112	155
10 Ma	116	163	115	163	127	174	127	174
1 Ma	133	183	131	183	144	194	144	194
100 ka	150	205	146	205	161	216	161	216
10 ka	169	230	162	230	180	241	180	241
1000 y	190	257	174	257	201	268	201	268
100 y	213	287	186	287	224	298	223	298
10 y	239	321	205	321	250	332	245	331
1 y	267	360	229	359	278	370	263	369
1 m	301	407	258	405	312	416	273	414
7 d	323	438	278	435	334	447	274	443
1 d	356	485	306	479	366	492	289	481
1 h	417	576	359	559	426	580	349	546
1 m	515	730	445	665	522	728	462	705
1 s	647	954	557	826	649	938	614	928

consolidation and compaction. Thus, while we test the estimates of C–O reordering kinetics versus these more established methods, in the future C–O reordering may become a measure against which other methods are compared.

4.2. Compilation of burial-temperature histories

We compiled burial temperature histories for strata from five sedimentary basins, ranging (roughly) from high-temperature to low-temperature: the Bird Spring Formation, Arrow Canyon, Nevada (Late Mississippian); the Cheremchanskian and Krasnopolyanskian Horizons, Ural Mountains, Russia (Early Pennsylvanian); the Grove Church Formation, Illinois (Late Mississippian); the Glenshaw Formation, West Virginia (Late Pennsylvanian); and the Fern Glen Formation, Missouri (Early Mississippian). Additionally, as a high-temperature end-member, we modeled the rapid burial and exhumation of the Carrara marble, initially comprised of marine carbonate rocks that were buried deeply enough to become part of a metamorphic core and metamorphosed to marble (Kligfield et al., 1986; Carmignani and Kligfield 1990; Fellin et al., 2007). When possible we used complete thermal histories determined by previous studies, for example a numerical hydrothermal fluid-flow model for the southern Illinois Basin in Rowan et al. (2002) and an apatite fission track and (U–Th)/He thermochronology record for the central Appalachian Basin in Reed et al. (2005). However, this was not possible for other basins and therefore we compiled basic thermal histories using published data from conodont color alteration, vitrinite reflectance, sediment decompaction, and geochemistry. Temperatures, times, uncertainties, and citations for all burial temperature histories are given in Tables S5–S10.

As part of this empirical comparison it is important to consider the range of uncertainty for each point used to construct thermal histories. The commonly used indices for burial temperature have errors arising from analytical methods (e.g., (U–Th)/He thermochronology; see Reed et al., 2005) and natural variability (e.g., conodont color alteration; see Epstein et al., 1977). Because of the relatively narrow band between ‘unaltered’ and ‘reordered’ states apparent in Fig. 4, a slight shift (within error) to warmer or cooler temperatures in the compiled burial histories could result in drastically different model predictions of apparent $T(\Delta_{47})$. This threshold behavior is discussed further in Section 4.3, but to give a sense of this feature in complex, natural systems we have modeled both ‘shallow’ and ‘deep’ scenarios. These represent the lower and upper bounds of uncertainty in our compilations and expose a limitation of these empirical data-model comparisons, as the scenarios often yield extreme $T(\Delta_{47})$ predictions (i.e., no reordering at the lower bound and ‘complete’ reordering at the higher bound). It should also be noted that uncertainty in the chronology of the thermal histories is as important in the models as uncertainty in burial temperatures, but for simplicity we only consider the latter.

4.3. Results: predicted reordering during burial versus observed $T(\Delta_{47})$

A schematic diagram demonstrating the behavior of the first-order approximation model in response to a simple, hypothetical burial and exhumation history is shown in Fig. 5. There are several distinct features of the burial trajectory predicted by the model. First, there is a period where clumped isotope reordering is ‘inactive’, coinciding with early burial, and original $T(\Delta_{47})$ values do not change. For a sample buried to sufficiently high temperatures this

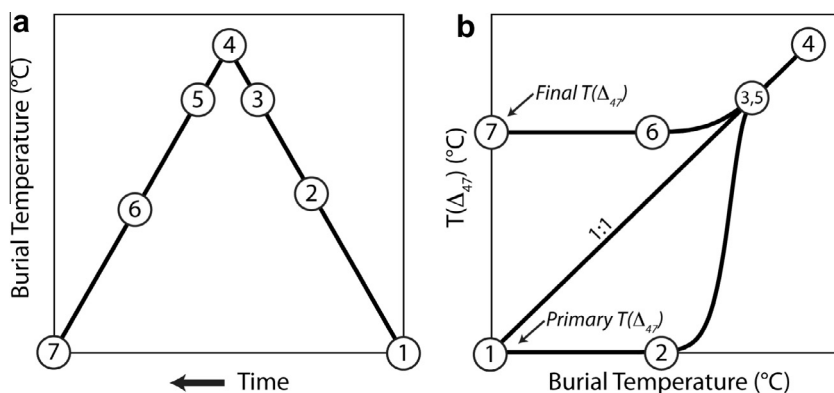


Fig. 5. A schematic guide to the features of the burial history (a) and $T(\Delta_{47})$ -burial T trajectories (b) predicted by the first-order approximation model for carbonate clumped isotope reordering. Points 1 → 2: Reordering ‘inactive’ during early burial. No change in $T(\Delta_{47})$ is predicted by the model. Points 2 → 3: Reordering becomes ‘active’ during further burial. Points 3 → 4: Reordering remains active, and the clumped isotope temperature of the sample is in equilibrium with the burial temperature. Points 4 → 5: The sample remains in equilibrium with the burial environment during retrograde cooling. Points 5 → 6: Reordering remains active during further cooling but is ‘closing’ with respect to the burial environment. Points 6 → 7: Reordering becomes inactive during late exhumation and apparent $T(\Delta_{47})$ is ‘locked in’. It should be noted that if a buried sample only reaches point 2 (that is, if burial temperatures do not reach the active region of the reordering curve) then the first-order approximation model predicts no change in original $T(\Delta_{47})$.

initial inactivity is followed by a period of rapid activation of reordering when the apparent $T(\Delta_{47})$ approaches equilibrium with the burial environment. With increasing temperature, $T(\Delta_{47})$ reaches equilibrium with the ambient temperature ($T(\Delta_{47}) = T$). Once the sample reaches this point of apparent thermal equilibrium it will continue to remain in equilibrium at all higher burial temperatures. During retrograde cooling the sample will again pass through the burial temperature equilibrium point and enter a phase where reordering is still active, but is ‘closing’ (i.e., apparent $T(\Delta_{47}) > T$). Eventually the sample will cool to a point where reordering is effectively closed and the mineral ‘locks in’ an apparent $T(\Delta_{47})$ value.

Modeled changes in brachiopod (and marble) clumped isotope compositions, expressed as apparent $T(\Delta_{47})$, are presented in Figs. 6 and 7 along with estimated burial temperature histories used in each of the models (from Tables S5–S10). The panels in each figure are arranged in order of highest $T(\Delta_{47})$ to lowest. Fig. 6 shows scenarios for the three highest $T(\Delta_{47})$ values, including the marble, and Fig. 7 shows the scenarios for the three lowest. In most cases three ‘burial trajectories’ are shown for each basin, with the upper and lower curves reflecting the uncertainty in the burial temperature estimates in our compilations. The yellow stars indicate the measured $T(\Delta_{47})$ from each basin and allow for direct comparison with the final model predictions.

In the six comparisons in Figs. 6 and 7 the models demonstrate at least one or more of the features described in Fig. 5, thereby capturing a range of responses from the reordering model. Overall, we observe a general (albeit inexact) correspondence between the measured $T(\Delta_{47})$ and the reordering model predictions. In the U.S. midcontinent, which has the coolest reconstructed burial temperatures, burial trajectories never reach the aforementioned activation period (Fig. 7f), whereas basins with high peak burial temperatures approach thermal equilibrium with the burial

environment, with final Δ_{47} values possibly determined by retrograde reordering and cooling rate during exhumation (Fig. 6d). The burial trajectory for the Carrara marble also shows this cooling rate dependence, and close correspondence between all of the modeled scenarios and the measured $T(\Delta_{47})$ (Fig. 6b).

This empirical test, however, is not without complications. Observed clumped isotope temperature from Arrow Canyon, NV are only compatible with the ‘deep’ burial scenario (Fig. 6c and d)—that is, the upper bound of the temperatures estimated from measured conodont color alteration index values of 2.0–2.5 (Martin et al., 2012)—and all of the model predictions from the Ural Mountains are cooler than the measured $T(\Delta_{47})$ (Fig. 6e and f). In Arrow Canyon these results suggest that carbonate clumped isotope studies may complement and refine existing maximum burial temperature estimates in the region as reordered brachiopod clumped isotope thermometry indicates at least a minimum burial temperature, thereby invalidating shallower burial histories (Fig. 6c and d). In the Ural Mountains the data-model mismatch highlights the lack of reliable burial information in the middle Uralian foredeep where our brachiopods were collected (Fig. 6e and f; Mii et al., 2001). However, it is also possible that data-model differences are the result of these brachiopod shells having different and thus far unrecognized clumped isotope reordering kinetics. We are continuing to conduct timed heating experiments on other brachiopod calcites to probe whether there are a range of susceptibilities to carbonate clumped isotope reordering, but the observation that two vastly different calcite samples (Permian brachiopod and hydrothermal optical calcite) have nearly identical kinetics (i.e., Fig. 3) suggests that compositionally similar minerals may have similar kinetics.

The wide range of possible trajectories predicted by the reordering model using published burial histories is best demonstrated by the data-model comparisons in the Illinois

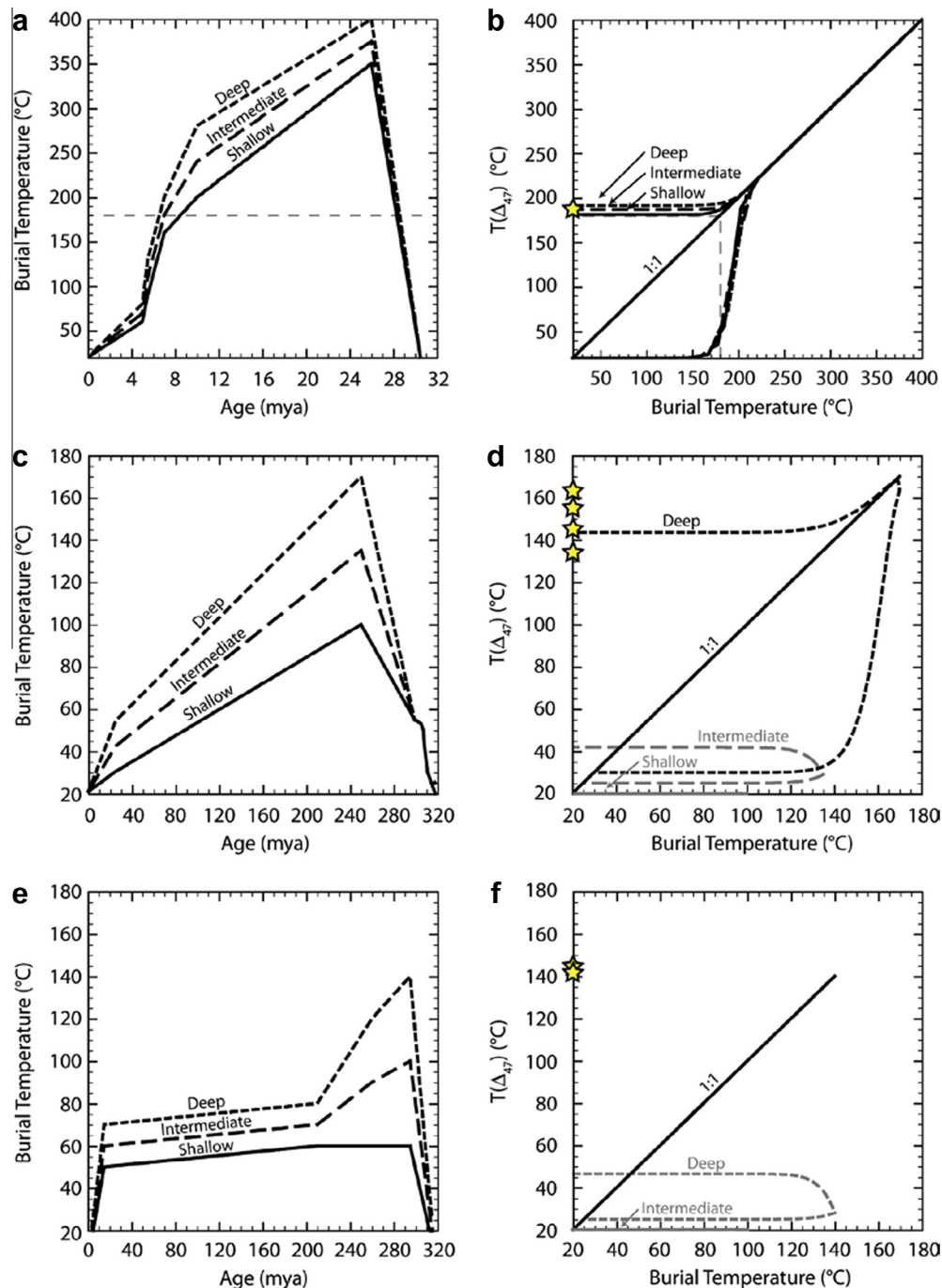


Fig. 6. Diagrams showing the compiled burial histories for samples with apparent $T(\Delta_{47})$ greater than 100 °C, including Carrara marble, and the modeled evolution of $T(\Delta_{47})$ during burial. Supporting data for burial temperature histories are presented in [Tables S5–S7](#) for the Carrara marble (a, b), brachiopods from Arrow Canyon, NV (c, d), and brachiopods from the Ural Mountains, Russia (e, f). For each location three curves are shown: an ‘intermediate’ curve representing published values, and ‘deep’ and ‘shallow’ curves representing uncertainty in the burial temperature estimates. The grayed lines in (d) and (f) are the model predictions that are invalidated by the measured $T(\Delta_{47})$ values (i.e., the values represent minimum burial temperatures). The clumped isotope reordering model for the Carrara marble used kinetic parameters from [Passey and Henkes \(2012\)](#) for the optical calcite, whereas the brachiopod models used parameters for the ‘first-order approximation model’ determined in this study. The gray dashed lines in (a) and (b) mark the axis boundaries in (c) through (f). Yellow stars in (b), (d), and (f) indicate measured clumped isotope temperatures ([Table 1](#)). (For interpretation of the references to colour in this figure legend, the reader is referred to the web version of this article.)

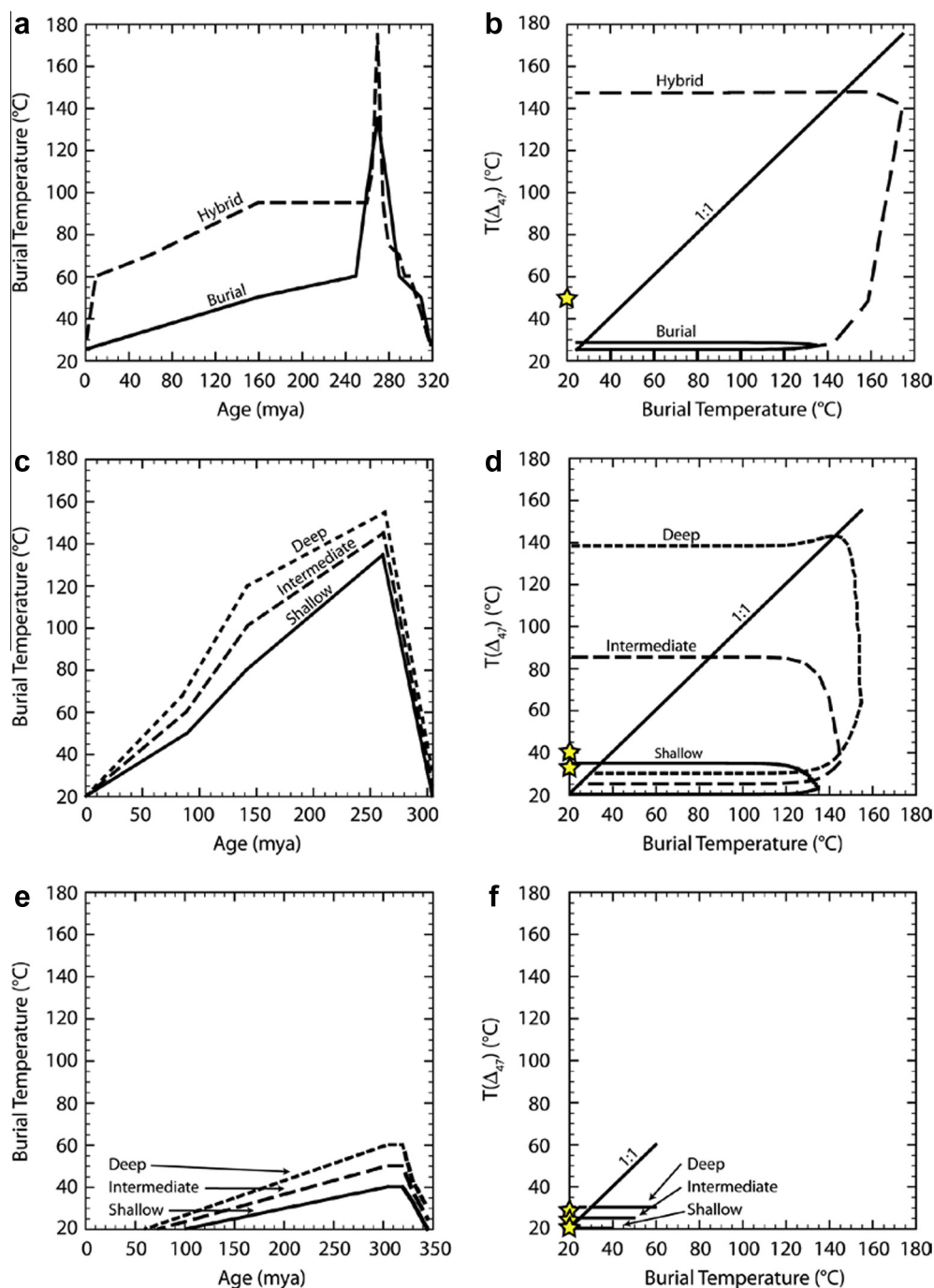


Fig. 7. Diagrams showing the compiled burial histories for samples with apparent $T(\Delta_{47})$ less than 100 °C and the modeled evolution of $T(\Delta_{47})$ during burial. Supporting data for burial temperature histories are presented in [Tables S8–S10](#) for brachiopods from the Illinois Basin (a, b), the Appalachian Basin, WV (c, d), and the U.S. midcontinent, MO (e, f). For each location three curves are shown: an ‘intermediate’ curve representing published values, and ‘deep’ and ‘shallow’ curves representing uncertainty in the burial temperature estimates. Yellow stars in (b), (d), and (f) indicate measured clumped isotope temperatures ([Table 1](#)). For the Illinois Basin we relied exclusively on modeled burial temperature histories of [Rowan et al. \(2002\)](#), who considered (1) a thermal history using sedimentary burial only (“burial”) and (2) a hybrid thermal history using burial depth and simulated hydrothermal fluid flow (“hybrid”). An intermediate burial scenario was not considered for this locality. (For interpretation of the references to colour in this figure legend, the reader is referred to the web version of this article.)

and Appalachian Basins. In both cases the measured $T(\Delta_{47})$ values are only consistent with the cooler burial temperature histories ([Fig. 7a–c](#)). In the Illinois Basin there is good

geologic and model-based evidence of late Paleozoic hydrothermal fluid flow, as shown by the thermal ‘pulse’ in [Fig. 7a](#). Because this pulse is relatively short-lived, the

modeled $T(\Delta_{47})$ is highly dependent on the maximum temperature of the fluid, and hence the wide range of predictions in Fig. 7b. In this case, additional clumped isotope measurements could help constrain the duration, geographic range, and peak temperature of this event due to the wide temperature–time sensitivity of clumped isotope reordering (Fig. 4).

To summarize, these data-model comparisons highlight a relationship between the burial temperature history of fossil brachiopod shell calcite and its measured carbonate clumped isotope composition. From the perspective of preservation of primary brachiopod paleotemperatures, these results suggest that Δ_{47} values are preserved at burial temperatures of less than ~ 100 – 120 °C; above those temperatures C–O bond reordering begins altering Δ_{47} values. This is illustrated in Fig. 8 where we used a simple ‘box car’ heating event lasting 60 million years and the first-order approximation model for WA-CB-13 to solve for the evolution of $T(\Delta_{47})$ at simulated burial temperatures from 100 to 160 °C. At 160 °C, the apparent $T(\Delta_{47})$ altered to 160 °C in ~ 15 million years, whereas at 100 °C there is no apparent change in $T(\Delta_{47})$. Intermediate burial temperatures show a range of final $T(\Delta_{47})$ between 28 and 137 °C, none of which reach apparent thermal equilibrium with the artificial burial environment after 60 million years. Translated to the geologic record, this behavior implies that carbonate fossils with burial temperature histories that fall within this intermediate temperature range may be expected to have a wide range of measured Δ_{47} values. In contrast, primary carbonate with burial temperatures that are lower

or higher than this range are expected to show, respectively, either no evidence of reordering or essentially complete reordering to higher $T(\Delta_{47})$ values, the latter reflecting cooling rate dependent ‘closure’ temperatures (e.g., Passey and Henkes, 2012). In the future, these observations may be exploited by measurement of natural brachiopod shells spanning a range of stratigraphic positions in a single basin as a tool for refining the dynamics of burial.

5. CONCLUSIONS AND AN OUTLOOK FOR FUTURE RESEARCH

A key conclusion from the laboratory reordering data and empirical comparisons presented in this study is constraining the burial temperatures capable of preserving of primary brachiopod paleotemperatures to less than ~ 100 °C for 10^6 – 10^8 year timescales. Also remarkable is the nearly identical carbonate clumped isotope reordering kinetics for two different types of calcite, well-preserved Permian brachiopod calcite and an optical calcite. The similar trace element content of these materials (Table S3; Fig. 1, Passey and Henkes, 2012) and the implication of ionic impurities in the creation of extrinsic crystallographic defects suggest that the bulk chemistry of calcite may, in part, determine its susceptibility or resistance to reordering. A positive relationship between trace element (Mn) content and the rate of O diffusion into the calcite lattice has been identified (Kronenberg et al., 1984), but similar effects on self-diffusion of C and O within a carbonate mineral are largely unknown. We note, however, that an experimentally heated calcite spar sample from Passey and Henkes (2012; NE-CC-1) had very different Mg and Mn contents and distinctly different reordering kinetics. A combination of future experiments and identification of naturally reordered samples will likely shed new light on the relationship between trace elements and reordering, and on the nature of C–O bond reordering itself.

This conclusion limits meaningful clumped isotope paleoclimate records to sedimentary basins with relatively shallow burial histories. Fortunately, we can screen the stratigraphic record for suitable burial histories prior to analysis. Thermal maturity index data and thermochronology studies exist for most basins throughout the world due to the economic importance of oil, gas, and coal resources, particularly (and fortuitously) in pre-Cenozoic strata. As was attempted in Section 4 of this study, compilations of these data prior to sampling for deep-time paleoclimate studies should allow for a ‘first-pass’ evaluation of primary $T(\Delta_{47})$ preservation with respect to clumped isotope reordering. Additionally, an understanding of the reordering reaction kinetics for other minerals commonly targeted for carbonate clumped isotope analysis – for example soil carbonates, mollusk shells, biogenic apatite, and dolomite – will further constrain the burial environments capable of preserving primary paleoclimate information over a range of timescales.

Finally, the clumped isotope composition of pristine, yet reordered brachiopod shells may be exploited and utilized as a low-temperature geothermometer, provided brachiopod calcite reordering kinetics are universal and appropriate

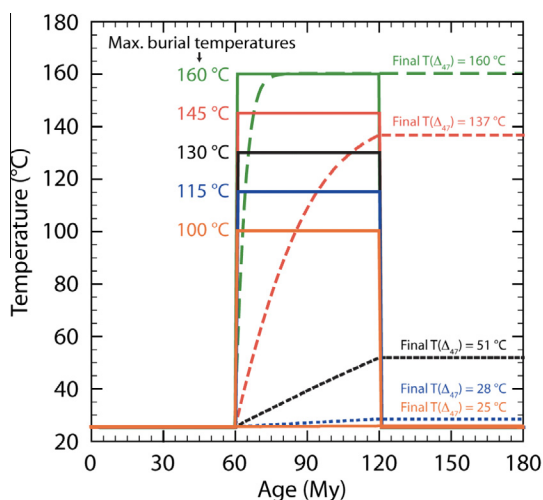


Fig. 8. Illustration of the threshold behavior of carbonate clumped isotope reordering for simple ‘box-car’ heating scenarios lasting 60 million years. The solid lines represent the temperature forcing used to solve the first-order approximation model and are in 15 °C increments from 100 to 160 °C. The dashed and dotted lines represent the model response at each time step, with the final indicated temperature (at 180 My) equivalent to a measured Δ_{47} temperature. At 100 °C maximum burial temperature there is no apparent change from the initial $T(\Delta_{47})$ (25 °C) whereas at 160 °C maximum burial temperature the model predicts complete reordering.

constraints can be placed on their geological context (e.g., age and stratigraphy). This approach would be similar to the inversion of low-temperature thermochronology data resulting in a set of temperature–time ‘paths’ or a single, best-fit path representing some statistical evaluation of the numerical models presented in this paper and measured $T(\Delta_{47})$ (Ketcham, 2005). Of course, this approach would require that the variation observed in Δ_{47} values would be solely determined by clumped isotope reordering processes and not simultaneously influenced by cryptic dissolution/reprecipitation diagenesis, which cannot be definitively ruled out for the natural and experimental brachiopods in this study.

Electron backscatter diffraction (EBSD) is a relatively new technique with increasing use in the study of diagenesis of fossil biocarbonates, including brachiopods. EBSD has been used to detect loss of primary crystallographic orientation with no apparent alteration of microstructures (Pérez-Huerta et al., 2007, 2012), presence of secondary mineralization and recrystallization not detected with other techniques (such as XRD; Cusack et al., 2008), and the presence of primary crystallographic information for paleoecological and phylogenetic applications (Grellet-Tinner et al., 2012; Dietrich et al., 2013). Ongoing analyses are expected to provide information on how EBSD observations of extant brachiopod shells compare with samples from the geologic record, and will probe micro-scale calcite dissolution/reprecipitation and diagenetic reorientation of otherwise ‘well-preserved’ calcite crystals. In the context of carbonate clumped isotope reordering, EBSD may be well-suited as a complementary method used to rule out the contribution of chemical diagenesis to apparent $T(\Delta_{47})$ changes. It may also be able to constrain the spatial scales over which C–O bond reordering occurs, to the extent that crystallite size may exert control over the maximum domain size of defect propagation. In future applied and experimental clumped isotope studies we envision ‘next generation’ sample screening techniques such as EBSD to be used in conjunction with traditional petrographic screening, as each method has equivalent trade-offs between analysis time and resolution.

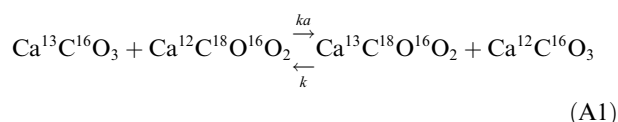
ACKNOWLEDGMENTS

We would like to thank Arthur Mory and David Haig for their assistance with collection of shell fragment WA-CB-13 and for sharing their insights on Permian strata in Western Australia, and Ken Livi for electron microprobe analyses. Ray Guillemette is acknowledged for his advice and assistance on petrographic screening. We also thank Andreas Kronenberg for discussions and insights about solid-state diffusion in calcite, and three anonymous reviewers for comments that helped improve the manuscript. This research was funded by a grant from the United States National Science Foundation (EAR-1227076, and in part from EAR-1118713), the American Chemical Society Petroleum Research Fund, and The Johns Hopkins University Department of Earth and Planetary Sciences. Samples were collected with prior support from the United States National Science Foundation (EAR-9304815, EAR-0003596, and EAR-0643309).

APPENDIX A.

Derivation of the transient defect/equilibrium defect model

Here we provide a full derivation of the ‘transient defect/equilibrium defect’ model for carbonate clumped isotope reordering as an alternative explanation (to the ‘first-order approximation’ model in Section 3.3) for the experimental observations in Fig. 3a and d. We can start with a more complete form of Eq. (1) to describe the reordering reaction:



where the reaction from left to right corresponds to the ordering reaction, and from right to left is the disordering reaction. For simplicity, we denote the species in Eq. (A1) as (from left to right) 61, 62, 63, and 60, in reference to the mass numbers of the carbonate ion in each species. Also, for simplicity we do not explicitly include ^{17}O and the isotopologues $^{12}\text{C}^{17}\text{O}^{18}\text{O}$, $\text{Ca}^{13}\text{C}^{17}\text{O}_2^{16}\text{O}$, and $\text{Ca}^{12}\text{C}^{17}\text{O}_3$, which together comprise only about 6.5% of mass 63 isotopologues (Ghosh et al. 2006a). The following derivation is based largely on Criss’ (1999, p. 140–142) treatment for the kinetics of isotopic exchange. The rate of change of the clumped species (mass 63) can be written as:

$$\frac{d63}{dt} = k\alpha[61][62] - k[63][60], \quad (\text{A2})$$

where the brackets denote fractional abundances ($[60] + [61] + [62] + [63] \approx 1$). Note that at equilibrium, the left term becomes zero, and α is the equilibrium constant:

$$\alpha_{eq} = \frac{[63]_{eq}[60]_{eq}}{[61]_{eq}[62]_{eq}}. \quad (\text{A3})$$

The isotopologue ratios normalized to mass 60 are:

$$R^{63} = \frac{[63]}{[60]}, R^{62} = \frac{[62]}{[60]}, R^{61} = \frac{[61]}{[60]} \quad (\text{A4})$$

Combining (A2) and (A4) yields:

$$\frac{d63}{dt} = k\alpha R^{61}R^{62}[60]^2 - kR^{63}[60]^2 \quad (\text{A5a})$$

Since the concentration of mass 60 is essentially constant, $[60]^2$ is constant and can be subsumed into k , so:

$$\frac{d63}{dt} = k(\alpha R^{61}R^{62} - R^{63}) \quad (\text{A5b})$$

Differentiation of R^{63} yields:

$$dR^{63} = \frac{d[63]}{[60]} - \frac{[63]d[60]}{[60]^2} \quad (\text{A6a})$$

Because $[63]$ is very small ($\sim 6.5 \times 10^{-5}$), and $d[60] = d[63]$ (from Eq. (A1)) and $[60]$ is close to 1, the second term on the right side is negligible compared to the first term on the right side. Thus:

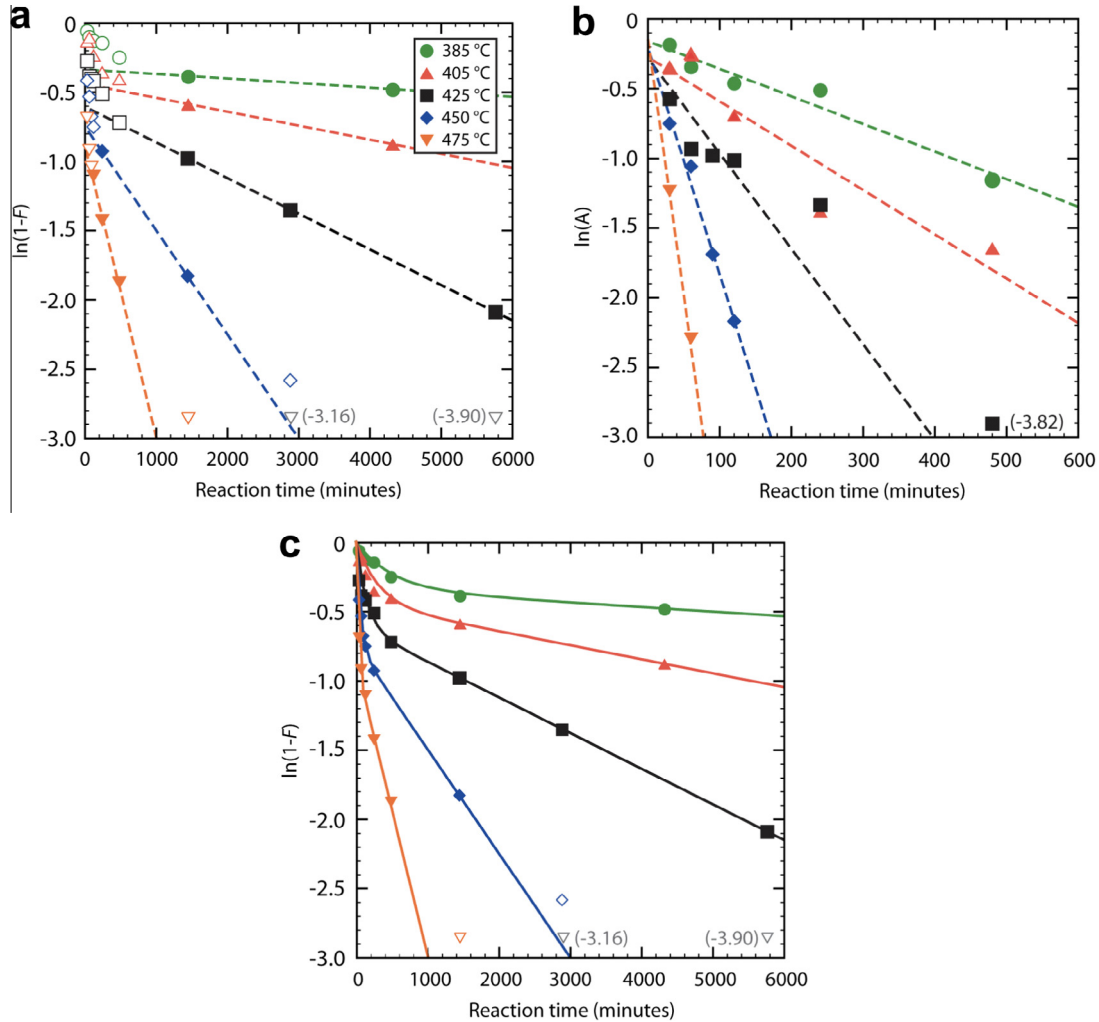


Fig. B1. The scheme for determining reaction rates constants for the transient defect/equilibrium defect model. (a) First-order reaction progress (i.e., equilibrium defect pool) and best-fit linear regressions plotted as a function of time. Empty symbols, which mostly represent early, non-first-order samples, are not included in the regressions. The temperatures of the heating experiments are indicated. Gray inverted triangle symbols for the 475 °C reaction plot off-axis and closely approach equilibrium, and thus are not suitable for inclusion in the regression. (b) Reaction progress of the early, non-first order data that represent the annealable transient defect pool. (c) Reaction progress data plotted with the full solutions to the transient defect/equilibrium defect model (Eq. (A15), solid lines) for each experimental temperature.

$$dR^{63} = \frac{d[63]}{[60]} \quad (\text{A6b})$$

Combining (A5b) and (A6b), and subsuming [60] into the rate constant, yields:

$$dR^{63} = -k(R^{63} - \alpha R^{61} R^{62}) dt \quad (\text{A7})$$

In a closed system, variation in R^{63} is due solely to deviation of R^{63} from the stochastic prediction. The natural range of this deviation is on the order of 1.5‰ (Eiler and Schauble, 2004), which corresponds to a change of 0.0001‰ (0.1 ppm) in the absolute abundance of mass 63 carbonate. According to Eq. (A1), the corresponding change in mass 61 and 62 carbonate is the same (~0.1 ppm), which amounts to ~0.009‰ and ~0.016‰ changes in R^{61} and R^{62} , respectively. Thus, compared to changes in R^{63} , changes in R^{61} and R^{62} due to reordering

reactions are negligible, and we can approximate these ratios as their equilibrium values. Combining (A7) and (A3)V thus yields:

$$dR^{63} = -k(R^{63} - R_{eq}^{63}) dt \quad (\text{A8})$$

where R_{eq}^{63} is the R^{63} ratio at thermodynamic equilibrium, and is therefore constant at any given temperature.

To account for the rapid initial reaction observed in the experimental data, we propose that the rate constant k is related to (1) a time-invariant pool of equilibrium defects of concentration D_e with an ability to effect C–O bond reordering (represented by k_e), and (2) a pool of transient defects of concentration D_d that decreases with time due to defect annealing, trapping, or other means of deactivation, with an ability to effect C–O bond reordering indicated by k_d . Thus equation A8 can be recast as:

$$\frac{dR^{63}}{R^{63} - R_{eq}^{63}} = -(k_c D_c + k_d D_d) dt \quad (A9)$$

Since D_c is constant, it can be subsumed into the rate constant k_c of the equilibrium defect pool. D_d is not constant, and although other models are imaginable, we assume that the rate of defect disappearance is proportional to the concentration of defects:

$$D_d = D_0 e^{-k_2 t} \quad (A10)$$

where D_0 is the initial defect concentration, and k_2 is a rate constant describing the loss of defects with time. Since D_0 is constant, it can be subsumed into k_d , and therefore:

$$\frac{dR^{63}}{R^{63} - R_{eq}^{63}} = -(k_c + k_d e^{-k_2 t}) dt \quad (A11)$$

Integration yields:

$$\ln(R_t^{63} - R_{eq}^{63}) = -k_c t + \frac{k_d}{k_c} e^{-k_2 t} + C \quad (A12)$$

At $t = 0$, $R_t^{63} = R_{init}^{63}$, the initial R^{63} of the sample, and therefore:

$$\ln(R_{init}^{63} - R_{eq}^{63}) = \frac{k_d}{k_c} + C \quad (A13)$$

Combining Eqs. (A12) and (A13) yields:

$$\ln\left(\frac{R_t^{63} - R_{eq}^{63}}{R_{init}^{63} - R_{eq}^{63}}\right) = -k_c t + \frac{k_d}{k_c} (e^{-k_2 t} - 1) \quad (A14)$$

which is approximately equivalent to (see [Passey and Henkes, 2012](#), Appendix A):

$$\ln\left(\frac{\Delta_{47}^t - \Delta_{47}^{eq}}{\Delta_{47}^{init} - \Delta_{47}^{eq}}\right) = -k_c t + \frac{k_d}{k_2} (e^{-k_2 t} - 1) \quad (A15)$$

All of the parameters on the left side of the equation can be determined by mass spectrometry (or provisionally inferred from theory in the case of Δ_{47}^{eq}), leaving the parameters k_c , k_d , and k_2 as unknowns.

APPENDIX B.

Determination of rate constants in the ‘transient defect/equilibrium defect’ model

As shown by Eq. (A15), the carbonate clumped isotope reordering reaction progress for any temperature is related to three rate constants: k_c , k_d , and k_2 . Here we describe an inverse ‘curve-stripping’ procedure for determining these rate constants that is analogous to the approach used to identify different half-lives in mixtures of radioisotopes ([Friedlander et al., 1981](#); see also [Appendix B of Passey and Henkes, 2012](#)). For convenience, we define a reaction progress term $\ln(1 - F)$ as:

$$\ln(1 - F) = \ln\left(\frac{\Delta_{47}^t - \Delta_{47}^{eq}}{\Delta_{47}^{init} - \Delta_{47}^{eq}}\right) = -k_c t + \frac{k_d}{k_c} (e^{-k_2 t} - 1) \quad (B1)$$

In the case where $k_2 \gg k_c$, the term $e^{-k_2 t}$ becomes negligible at long times t , and Eq. (B1) reduces to:

$$\ln(1 - F) = -k_c t - \frac{k_d}{k_2} \quad (B2)$$

Therefore a plot of $\ln(1 - F)$ versus t will produce straight line arrays whose slope correspond to the temperature-dependent values of $-k_c$, and whose intercepts equal $-k_d/k_2$. [Fig. B1a](#) shows that this is true for WA-CB-13 at the experimental temperatures, indicating that $k_2 \gg k_c$ for this material. Note that while the mathematics differ, procedurally this is equivalent to the regressions in the first-order approximation model ([Fig. 3a and b](#); see also [Passey and Henkes, 2012](#)).

Table B1

Rate constants and Arrhenius parameters determined for the transient defect/equilibrium defect model using the Permian brachiopod calcite WA-CB-13.

Reaction T (°C)	Slope (=-k _c) (s ⁻¹)	Intercept (=-k _d /k ₂)	R ²	SRX points used*	
<i>Equilibrium defect component</i>					
385	-5.48 × 10 ⁻⁷	-0.34	—	037, 042	
405	-1.68 × 10 ⁻⁶	-0.44	—	041, 044	
425	-4.29 × 10 ⁻⁶	-0.61	1.00	012, 013, 014	
450	-1.25 × 10 ⁻⁵	-0.74	—	020, 031	
475	-3.50 × 10 ⁻⁵	-0.87	0.99	017, 021, 029	
k _c Arrhenius parameters: E _a = 187.6 ± 2.7 kJ/mol; K ₀ = 4.5 × 10 ⁸ s ⁻¹ [(+27.14/-1.1)×10 ⁹]; R ² = 0.999					
Reaction T (°C)	Slope (=-k ₂) (s ⁻¹)	Intercept	Calculated k _d (s ⁻¹)	R ²	SRX points used*
<i>Transient defect component</i>					
385	-3.30 × 10 ⁻⁵	-0.16	1.12 × 10 ⁻⁵	0.95	034, 036, 040, 043, 047
405	-5.30 × 10 ⁻⁵	-0.27	2.35 × 10 ⁻⁵	0.88	033, 035, 038, 045, 046
425	-1.14 × 10 ⁻⁴	-0.28	6.92 × 10 ⁻⁵	0.93	006, 007, 008, 009, 010, 011
450	-2.71 × 10 ⁻⁴	-0.19	2.02 × 10 ⁻⁴	0.98	019, 023, 025, 032
475	-6.14 × 10 ⁻⁴	-0.11	5.39 × 10 ⁻⁴	1.00	016, 026, 027
k _d Arrhenius parameters: E _a = 180.0 ± 5.7 kJ/mol; K ₀ = 2.0 × 10 ⁹ s ⁻¹ [(+34.5/-8.1)×10 ⁸]; R ² = 0.997					
k ₂ Arrhenius parameters: E _a = 136.1 ± 3.7 kJ/mol; K ₀ = 1.8 × 10 ⁶ s ⁻¹ [(+13.1/-7.2)×10 ⁵]; R ² = 0.993					

Note: ± values are the standard errors of error weighted, best-fit linear regressions using the statistical software package JMP.

* Stable isotope data provided in [Table S4](#).

Table B2

Rate constants and Arrhenius parameters determined for the transient defect/equilibrium defect model using the optical calcite MGB-CC-1.

Reaction T (°C)	Slope ($=-k_c$) (s $^{-1}$)	Intercept ($=-k_d/k_2$)	R^2	SRX points used*	
<i>Equilibrium defect component</i>					
385	-3.18×10^{-7}	-0.27	—	181, 189	
405	-1.40×10^{-6}	-0.32	0.99	169, 173, 177	
425	-2.00×10^{-6}	-0.59	0.97	149, 150, 151, 153	
450	-7.95×10^{-6}	-0.88	0.91	144, 145, 147, 148	
475	$-298. \times 10^{-5}$	-0.79	0.97	112, 113, 114, 115	
k_c Arrhenius parameters: $E_a = 196.6 \pm 19.1$ kJ/mol; $K_0 = 1.4 \times 10^9$ s $^{-1}$ [(+37/-1.3) $\times 10^9$]; $R^2 = 0.97$					
Reaction T (°C)	Slope ($=-k_2$) (s $^{-1}$)	Intercept	Calculated k_d (s $^{-1}$)	R^2	SRX points used*
<i>Transient defect component</i>					
385	-4.43×10^{-5}	-0.31	1.19×10^{-5}	0.47	182, 183, 185, 187
405	-7.68×10^{-5}	-0.30	2.48×10^{-5}	0.76	168, 171, 175, 176, 178, 179
425	-7.07×10^{-5}	-0.46	4.15×10^{-5}	0.55	152, 154, 166, 167, 170, 172, 174
450	-1.29×10^{-4}	-0.33	1.14×10^{-4}	—	143, 146
k_d Arrhenius parameters: $E_a = 133.3 \pm 11.9$ kJ/mol; $K_0 = 4.5 \times 10^5$ s $^{-1}$ [(+30.8/-3.9) $\times 10^5$]; $R^2 = 0.999$					
k_2 Arrhenius parameters: $E_a = 47.9 \pm 21.2$ kJ/mol; $K_0 = 3.2 \times 10^{-1}$ s $^{-1}$ [(+1.3/-0.3) $\times 10^1$]; $R^2 = 0.940$					

Note: \pm values are the standard errors of error weighted, best-fit linear regressions using the statistical software package JMP.

* Stable isotope data from [Passey and Henkes \(2012\)](#).

In practice, when selecting the points to define the equilibrium defect (linear) behavior, it is important to consider that some points at earlier times t may still reflect the evolving contribution of the transient pool of defects (i.e., when the transient pool is active), and thus should not be included in the regression (Fig. B1a). Conversely, at very long experimental times t and high temperatures T the Δ_{47} values may approach the equilibrium Δ_{47} composition, where analytical error has an increasingly large influence in the error of calculated $\ln(1-F)$ values (gray data in Fig. B1a). Thus, it is important to establish a cut-off value for $\ln(1-F)$ below which values are excluded from the regression. Admittedly, selection of a cut-off value is somewhat arbitrary, but here we use a value of -2.5 , which corresponds to the approximate $\ln(1-F)$ for a sample with $\Delta_{47} = \Delta_{47}^{equil} + 1\sigma$ (where 1σ is the analytical precision). We note that the exact value of Δ_{47}^{equil} used is dependent on the experimental temperature, so the exact $\ln(1-F)$ value will vary slightly.

With values of k_c and k_d/k_2 determined, the influence of the k_c pool is then added back to each data point, resulting in the quantity $\ln(1-F)'$:

$$\ln(1-F)' = \ln(1-F) + k_c t = \frac{k_d}{k_2} (e^{-k_2 t} - 1) \quad (B3)$$

Simply stated, $\ln(1-F)'$ represents the progress of reordering due only to the transient defect pool. Eq. (B3) can be rearranged to solve for k_2 in terms of $\ln(1-F)'$ and the ratio k_d/k_2 :

$$k_2 t = -\ln \left[\frac{k_2}{k_d} \left(\ln(1-F)' + \frac{k_d}{k_2} \right) \right] = -\ln(A) \quad (B4)$$

where A is substituted for the terms inside the brackets. Therefore, a plot of $\ln(A)$ versus t will produce straight line arrays whose slopes correspond to the temperature-dependent values of $-k_2$ (Fig. B1b). Values of k_d are calculated using k_2 values and the ratio k_d/k_2 . Finally, the Arrhenius relation (Eq. (3)) is used to determine the activation energies and frequency factors of each component. Table B1 summarizes the rate constants and Arrhenius parameters

determined for WA-CB-13, the Permian brachiopod calcite, and Table B2 summarizes the rate constants and Arrhenius parameter determined for MGB-CC-1, an optical calcite from [Passey and Henkes \(2012\)](#).

From Tables B1 and B2 it can be seen that the regressions for the k_c component are generally good, however, for WA-CB-13 many of the regressions are only defined by two points. Regressions for the k_2 component are excellent for WA-CB-13, but much less so for MGB-CC-1. In future experiments these uncertainties may be remedied by further experimentation, particularly in the early and late t range, and greater analytical replication (i.e., $n > 1-2$, Table S4). Also troubling is the fact that while equation B4 predicts that the intercept of $\ln(A)$ versus t should be zero, we observe intercepts as low as -0.5 (Tables B1 and B2, Fig. B1b). This may indicate the presence of an additional, unrecognized reordering component accounting for $\sim 5-10\%$ of the total reordering signal.

Finally, Fig. B1c shows that the forward model based on the derived Arrhenius parameters (Eq. (A15)) closely reproduces the observed data for WA-CB-13, with the exception of some data-model mismatch in the earliest reaction. This may be related to the non-zero intercept in the $\ln(A)$ versus t regressions. Nevertheless, we view the model as being successful at predicting the observed reordering behavior.

APPENDIX C. SUPPLEMENTARY DATA

Supplementary data associated with this article can be found, in the online version, at <http://dx.doi.org/10.1016/j.gca.2014.04.040>.

REFERENCES

- Adlis D. S., Grossman E. L., Yancey T. E. and McLerran R. D. (1998) Isotope stratigraphy and paleodepth changes of Pennsylvanian cyclical sedimentary deposits. *Palaio* **3**, 487–506.
- Affek H. P. and Eiler J. M. (2006) Abundance of mass 47 CO₂ in urban air, car exhaust, and human breath. *Geochim. Cosmochim. Acta* **70**, 1–12.

- Anderson T. F. (1969) Self-diffusion of carbon and oxygen in calcite by isotope exchange with carbon dioxide. *J. Geophys. Res.* **74**, 3918–3932.
- Brand U., Posenato R., Came R., Affek H., Angiolini L., Azmy K. and Farabegoli E. (2012) The end-Permian mass extinction: A rapid volcanic CO₂ and CH₄-climatic catastrophe. *Chem. Geol.* **322–323**, 121–144.
- Came R. E., Eiler J. M., Veizer J., Azmy K., Brand U. and Weidman C. R. (2007) Coupling of surface temperatures and atmospheric CO₂ concentrations during the Palaeozoic era. *Nature* **449**, 198–201.
- Carmignani L. and Kligfield R. (1990) Crustal extension in the northern Apennines: The transition from compression to extension in the Alpi Apuane core complex. *Tectonics* **9**, 1275–1303.
- Carpenter S. L. and Lohmann K. C. (1995) $\Delta^{18}\text{O}$ and $\delta^{13}\text{C}$ values of modern brachiopod shells. *Geochim. Cosmochim. Acta* **59**, 3749–3764.
- Castaño J. R. and Sparks D. M. (1974) Interpretation of vitrinite reflectance measurements in sedimentary rocks and determination of burial history using vitrinite reflectance and authigenic minerals. *Geol. Soc. Am. Spec. Paper* **153**, 31–52.
- Chacko T., Mayeda T. K., Clayton R. N. and Goldsmith J. R. (1991) Oxygen and carbon isotope fractionations between CO₂ and calcite. *Geochim. Cosmochim. Acta* **55**, 2867–2882.
- Cole D. R. and Chakraborty S. (2001) Rates and mechanisms of isotope exchange. *Rev. Mineral. Geochem.* **43**, 83–223.
- Compston W. (1960) The carbon isotopic composition of certain marine invertebrates and coals from the Australian Permian. *Geochim. Cosmochim. Acta* **18**, 1–22.
- Criss R. E. (1999) *Principles of stable isotope distribution*. Oxford University Press, New York.
- Cusack M., Dauphin Y., Chung P., Pérez-Huerta A. and Cuif J.-P. (2008) Multiscale structure of calcite fibres of the shell of the brachiopod *Terebratulina retusa*. *J. Struct. Biol.* **164**, 96–100.
- Dennis K. J. and Schrag D. P. (2010) Clumped isotope thermometry of carbonates as an indicator of diagenetic alteration. *Geochim. Cosmochim. Acta* **74**, 4110–4122.
- Dennis K. J., Affek H. P., Passey B. H., Schrag D. P. and Eiler J. M. (2011) Defining an absolute reference frame for ‘clumped’ isotope studies of CO₂. *Geochim. Cosmochim. Acta* **75**, 7117–7131.
- Dennis K. J., Cochran J. K., Landman N. H. and Schrag D. P. (2013) The climate of the Late Cretaceous: New insights from the application of the carbonate clumped isotope thermometer to Western Interior Seaway macrofossil. *Earth Planet. Sci. Lett.* **362**, 51–65.
- Dietrich D., Lampke T. and Rößler R. (2013) A microstructure study on silicified wood from the Permian petrified forest of Chemnitz. *Paläont. Zeitsch.* **87**, 397–407.
- Dixon M. D. and Haig D. W. (2004) Foraminifera and their habitats within a cool-water carbonate succession following glaciation, Early Permian (Sakmarian), Western Australia. *J. Foramin. Res.* **34**, 308–324.
- Donelick R. A., O’Sullivan P. B. and Ketcham R. A. (2005) Apatite fission-track analysis. *Rev. Mineral. Geochem.* **58**, 49–94.
- Eiler J. M. (2011) Paleoclimate reconstruction using carbonate clumped isotope thermometry. *Quater. Sci. Rev.* **30**, 3575–3588.
- Eiler J. M. and Schauble E. (2004) $^{18}\text{O}^{13}\text{C}^{16}\text{O}$ in Earth’s atmosphere. *Geochim. Cosmochim. Acta* **68**, 4767–4777.
- Epstein A. G., Epstein J. B., Harris L. D. (1977) Conodont color alteration – an index to organic metamorphism. Geological Survey Professional Paper 995, Washington.
- Farver J. R. (1994) Oxygen self-diffusion in calcite: Dependence on temperature and water fugacity. *Earth Planet. Sci. Lett.* **121**, 575–587.
- Fellin M. G., Reiners P. W., Brandon M. T., Wuthrich E., Balestrieri M. L. and Molli G. (2007) Thermochronologic evidence for the exhumational history of the Alpi Apuane metamorphic core complex, northern Apennines, Italy. *Tectonics* **26**, TC6015.
- Finnegan S., Bergmann K., Eiler J. M., Jones D. S., Fike D. A., Eisenman I., Hughes N. C., Tripathi A. K. and Fischer W. W. (2011) The magnitude and duration of Late Ordovician–Early Silurian glaciation. *Science* **331**, 903–906.
- Flake R. C. (2011) Circulation of North American epicontinental seas during the Carboniferous using stable isotope and trace element analyses of brachiopod shells. M. S. Thesis, Texas A&M Univ.
- Friedlander G., Kennedy J. W., Macias E. S. and Miller J. M. (1981) *Nuclear and radiochemistry*. Wiley, New York.
- Ghosh P., Garzione C. N. and Eiler J. M. (2006a) Rapid uplift of the Altiplano revealed through ^{13}C – ^{18}O bonds in paleosol carbonates. *Science* **311**, 511–515.
- Ghosh P., Adkins J., Affek H., Balta B., Guo W., Schauble E. A., Schrag D. and Eiler J. M. (2006b) ^{13}C – ^{18}O bonds in carbonate minerals: a new kind of paleothermometer. *Geochim. Cosmochim. Acta* **70**, 1439–1456.
- Grellet-Tinner G., Murelaga X., Larrasoana J. C., Silveira L. F., Olivares M., Ortega L. A., Trimby P. W. and Pascual A. (2012) The first occurrence in the fossil record of an aquatic avian twig-nest with Phoenicopteriformes eggs: evolutionary implications. *PLOS One* **7**, e46972.
- Grossman E. L. (2012a) Applying oxygen isotope paleothermometry in deep time. In *Reconstructing Earth’s Deep-Time Climate* (eds. L. Ivany and B. Huber). The Paleontological Society Papers 18, 39–67.
- Grossman E. L. (2012b) Ch. 10. Oxygen isotope stratigraphy. In *The Geologic Time Scale 2012* (eds. E. M. Gradstein, J. G. Ogg, M. Schmitz and G. Ogg). Elsevier, pp. 195–220.
- Grossman E. L., Mii H.-S., Zhang C. and Yancey T. E. (1996) Chemical variation in Pennsylvanian brachiopod shells—diagenetic, taxonomic, microstructural, and seasonal effects. *J. Sed. Res.* **66**, 1011–1022.
- Guo W., Mosenfelder J. L., Goddard, III, W. A. and Eiler J. M. (2009) Isotopic fractionations associated with phosphoric acid digestion of carbonate minerals: Insights from first-principles theoretical modeling and clumped isotope measurements. *Geochim. Cosmochim. Acta* **73**, 7203–7225.
- Henkes G. A., Passey B. H., Wanamaker, Jr., A. D., Grossman E. L., Ambrose, Jr., W. G. and Carroll M. L. (2013) Carbonate clumped isotope compositions of modern marine mollusk and brachiopod shells. *Geochim. Cosmochim. Acta* **106**, 307–325.
- Joachimski M. M., Breisig S., Buggisch W., Talent J. A., Mawson R., Gereke M., Morrow J. R., Day J. and Weddige K. (2009) Devonian climate and reef evolution: Insights from oxygen isotopes in apatite. *Earth Planet. Sci. Lett.* **284**, 599–609.
- Jones T. E., Grossman E. L. and Yancey T. E. (2003) Exploring the stable isotope record of global change and paleoclimate: the mid-Carboniferous GSSP (Arrow Canyon, Nevada) and the Ural Mountains, Russia. *Geol. Soc. Amer. Abs.* **35**, 254.
- Keating-Bitonti C. R., Ivany L. C., Affek H. P., Douglas P. and Samson S. D. (2011) Warm, not super-hot, temperatures in the early Eocene subtropics. *Geology* **39**, 771–774.
- Ketcham R. A. (2005) Forward and inverse modeling of low-temperature thermochronometry data. *Rev. Mineral. Geochem.* **58**, 275–314.

- Kim S.-T. and O'Neil J. R. (1997) Equilibrium and nonequilibrium oxygen isotope effects in synthetic carbonates. *Geochim. Cosmochim. Acta* **61**, 3461–3475.
- Kittel C. (2005) *Introduction to Solid State Physics*, 8th ed. John Wiley & Sons Inc, New Jersey.
- Kligfield R., Hunziker J. and Dallmeyer R. D. (1986) Dating of deformation phases using K–Ar and $^{40}\text{Ar}/^{39}\text{Ar}$ techniques: results from the Northern Apennines. *J. Struct. Geol.* **8**, 781–798.
- Kronenberg A. K., Yund R. A. and Giletti B. J. (1984) Carbon and oxygen diffusion in calcite: Effects of Mn content and $P_{\text{H}_2\text{O}}$. *Phys. Chem. Minerals* **11**, 101–112.
- Labotka T. C., Cole D. R., Fayek M. T. and Chacko T. (2011) An experimental study of the diffusion of C and O in calcite in mixed CO_2 – H_2O fluids. *Am. Mineral.* **96**, 1262–1269.
- Land L. S. (1995) Oxygen and carbon isotopic composition of Ordovician brachiopods: implications for coeval seawater: discussion. *Geochim. Cosmochim. Acta* **59**, 2843–2844.
- Lasaga A. C. (1998) *Kinetic Theory in the Earth Sciences*. Princeton University Press, New Jersey.
- Martin L. G., Montanez I. P. and Bishop J. W. (2012) A paleotropical carbonate-dominated archive of Carboniferous icehouse dynamics, Bird Spring Fm., Southern Great Basin, USA. *Palaeogeogr. Palaeoclimatol. Palaeoecol.* **329–330**, 64–82.
- Mii H.-S., Grossman E. L. and Yancey T. E. (1997) Stable carbon and oxygen isotope shifts in Permian seas of West Spitsbergen—global change or diagenetic artifact? *Geology* **25**, 227–230.
- Mii H.-S., Grossman E. L. and Yancey T. E. (1999) Carboniferous isotope stratigraphies of North America: Implications for Carboniferous paleoceanography and Mississippian glaciation. *Geol. Soc. Am. Bull.* **111**, 960–973.
- Mii H.-S., Grossman E. L., Yancey T. E., Chuvashov B. and Egorov A. (2001) Isotopic records of brachiopod shells from the Russian Platform – evidence for the onset of mid-Carboniferous glaciation. *Chem. Geol.* **175**, 133–147.
- Mory A. J. and Haig D. W. (2011) Permian–Carboniferous geology of the Northern Perth and Southern Carnarvon basins, Western Australia – a field guide. Geological Survey of Western Australia, Perth.
- O'Neil J. R., Clayton R. N. and Mayeda T. K. (1969) Oxygen isotope fractionation in divalent metal carbonates. *J. Chem. Phys.* **51**, 5547–5558.
- Passey B. H. and Henkes G. A. (2012) Carbonate clumped isotope bond reordering and geospeedometry. *Earth Planet. Sci. Lett.* **351–352**, 223–236.
- Passey B. H., Levin N. E., Cerling T. E., Brown F. H. and Eiler J. M. (2010) High-temperature environments of human evolution in East Africa based on bond ordering in paleosol carbonates. *Proc. Natl. Acad. Sci. USA* **107**, 11245–11249.
- Pérez-Huerta A., Cusack M. and England J. (2007) Crystallography and diagenesis in fossil craniid brachiopods. *Palaeontology* **50**, 757–763.
- Pérez-Huerta A., Cusack M. and Méndez C. A. (2012) Preliminary assessment of the use of electron backscatter diffraction (EBSD) in conodonts. *Lethaia* **45**, 253–258.
- Popp B. N., Anderson T. F. and Sandberg P. A. (1986) Brachiopods as indicators of original isotopic compositions in some Paleozoic limestones. *Geol. Soc. Am. Bull.* **97**, 1262–1269.
- Preston-Thomas H. (1990) The international temperature scale of 1990 (ITS-90). *Metrologia* **27**, 3–10.
- Price G. D. and Passey B. H. (2013) Dynamic polar climate in a greenhouse world: evidence from clumped isotope thermometry of Early Cretaceous belemnites. *Geology* **41**, 923–926.
- Ravaux J., Hamel G., Zbinden M., Tasiemski A. A., Boutet I., Léger N., Tanguy A., Jollivet D. and Shillito B. (2013) Thermal limit for metazoan life in question: *In vivo* heat tolerance of the Pompeii worm. *PLOS One* **8**, e64074.
- Reed J. S., Spotila J. A., Eriksson K. A. and Bodnar R. J. (2005) Burial and exhumation history of Pennsylvanian strata, central Appalachian basin: an integrated study. *Basin Res.* **17**, 259–268.
- Rowan E. L., Goldhaber M. B. and Hatch J. R. (2002) Regional fluid flow as a factor in the thermal history of the Illinois Basin: Constrains from fluid inclusions and the maturity of Pennsylvanian coals. *AAPG Bull.* **86**, 257–277.
- Schauble E. A., Ghosh P. and Eiler J. M. (2006) Preferential formation of ^{13}C – ^{18}O bonds in carbonate minerals, estimated using first principles lattice dynamics. *Geochim. Cosmochim. Acta* **70**, 2510–2529.
- Sheehan P. M. (2001) The late Ordovician mass extinction. *Annu. Rev. Earth Planet. Sci.* **29**, 331–364.
- Trotter J. A., Williams I. S., Barnes C. R., Lécuyer C. and Nicoll R. S. (2008) Did cooling oceans trigger Ordovician biodiversification? Evidence from conodont thermometry. *Science* **321**, 550–554.
- Veizer J. (1995) Oxygen and carbon isotopic composition of Ordovician brachiopods: implications for coeval seawater: Reply. *Geochim. Cosmochim. Acta* **59**, 2845–2846.
- Veizer J., Fritz P. and Jones B. (1986) Geochemistry of brachiopods: oxygen and carbon isotopic records of Paleozoic oceans. *Geochim. Cosmochim. Acta* **50**, 1679–1696.
- Veizer J., Ala D., Azmy K., Bruckschen P., Buhl D., Bruhn F., Carden G. A. F., Diener A., Ebner S., Godderis Y., Jasper T., Korte C., Pawellek F., Podlaha O. G. and Strauss H. (1999) $^{87}\text{Sr}/^{86}\text{Sr}$, $\delta^{13}\text{C}$ and $\delta^{18}\text{O}$ evolution of Phanerozoic seawater. *Chem. Geol.* **161**, 59–88.
- Zhang Y. (2010) Diffusion in Minerals and Melts: Theoretical Background. *Rev. Mineral. Geochem.* **72**, 5–59.

Associate editor: Miryam Bar-Matthews